Article:
Zhu, J., Shao, W., Huang, W. et al. (5 more authors) (2024) Nanostructure evolution and surface modification mechanism of Cr ion-implanted single-crystal iron: insights from molecular dynamics simulations. Journal of Materials Science, 59 (23). pp. 10324-10346. ISSN 0022-2461

https://doi.org/10.1007/s10853-024-09804-0

Nanostructure evolution and surface modification mechanism of Cr ion implanted single crystal iron: insights from molecular dynamics simulations

Jiangping Zhu[1], Wen Shao[1,*], Weiwei Huang[1], Jinyuan Tang[1], Tingting Jiang[1], Yuansheng Zhou[1], Xiaocheng Shen[1], Dimitrios Kontziampasis[2,3]

[1]*State Key Laboratory of Precision Manufacturing for Extreme Service Performance, College of Mechanical and Electrical Engineering, Central South University, Changsha, Hunan 410083, China*

[2]*School of Science and Engineering, University of Dundee, Dundee DD1 4HN, UK*

[3]*Dundee International Institute of Central South University, Central South University, Changsha, Hunan 410013, China*

Abstract: An advanced molecular dynamics (MD) model for Cr ion implantation of single crystal iron was proposed and its effectiveness was verified through SRIM calculations. The model systematically investigated the effects of Cr ion implantation energy and dose on surface morphology, ion distribution, surface damage, dislocation evolution and residual stress. The results clearly showed that the increment of implantation energy could significantly improve the surface roughness of the sample. Furthermore, the implantation energy proved crucial in determining the depth and extent of the modification layer. The escalation in implantation dose led to a progressive saturation of internal defects and the amorphous structure within the sample, with the saturation value being contingent upon the implantation energy. Thermal spike effects and recrystallization predominantly contribute to dynamic damage at elevated implantation energies. Conversely, in the context of low-energy implantation, a sufficiently high dose may facilitate the production of dislocations. Crucially, the underlying mechanism of dislocation loop evolution has been elucidated. Primarily, residual compressive stress arises from lattice distortion and phase transformation, with both its magnitude and penetration depth escalating in correlation with energy levels. Furthermore, annealing plays a pivotal role in diminishing residual compressive stress.

* Corresponding author.

E-mail address: wen.shao@csu.edu.cn, shaowen_2013@163.com (W. Shao).

Keywords: Ion implantation; Molecular dynamics; Single crystal iron; Nanostructure evolution; Residual stress

1. Introduction

In the field of material science, the exploration and development of advanced materials with optimized performance continuously propel the boundaries of technological innovation. On one hand, the drawbacks of materials can be addressed by finding materials with exceptional characteristics to meet the demands of various applications [1, 2]. On the other hand, the original materials can be modified to obtain superior properties through special technological methods, such as heat treatment, doping, and the addition of a second phase [3-7]. Ion implantation is a blooming and widely used material surface modification technology. It involves the implant of specific ions into solid material with a certain energy, resulting in significant changes in the physical and chemical properties of the surface of the solid material, thus improving its surface properties [8].

In recent years, there has been significant progress in the surface modification of ion-implanted metallic materials as reported in literature. Jin et al. [9, 10] studied the effect of ion implantation on the surface mechanical properties of Cr4Mo4Ni4V and Cronidur30 bearing steel, through nanoindentation, friction, and wear and fatigue life tests. The results proven that the co-implantation of N + Zr ions significantly improved the surface hardness, friction and wear resistance, and thermal contact fatigue resistance of Cr4Mo4Ni4V bearing steel. Especially in the case of the median fatigue life it was found to be increased by approximately 5 times. Ion implantation into Cronidur30 bearing steel results in the increase of the surface nano-hardness. Specifically, for the cases of Ti ion implantation and Ti + Cr double ion implantation, Cronidur30 is 1.2 and 1.3 times harder respectively, comparing to non-implanted samples. Considering wear resistance, if one compares the wear life of Cronidur30 after Ti + Cr dual ion implantation, this appears as 2 times and 10 times higher than the case of Ti ion implantation and non-implantation sample, respectively. Additionally, the same group studied the enhancement mechanism of ion implantation using numerous characterization test methods. Levintant-Zayonts et al. [11] showed that the hardness

of D6A and C75S spring steels implanted with N ions is approximately 3 times that of non-implanted ones. Simultaneously, N ion implantation changed the wear mechanism, resulting in increased wear resistance of the implanted samples. Wei et al. [12] studied the effect of Cr ion implantation on the surface roughness, nano-hardness, and fatigue life of TC18 alloy. It was proven that ion implantation led to bulges and pits on the surface of the tested samples. The surface roughness and nano-hardness initially increased first, but subsequently decreased with the increase of implantation dose. When the implantation dose was 3.56×10^{16} ions/cm^2, the fatigue strength increased from 407 MPa to 413 MPa. Ryabchikov et al. [13] reported the formation of a uniform intermetallic Al3Ti layer in an aluminum sample implanted with a Ti plasma with an average energy of 3 keV using a vacuum arc evaporator. Subsequently, using nanoindentation and dry friction, they found that the hardness of the Al3Ti surface layer increased from 0.4 GPa (for the undoped Al) to ~ 4 GPa, while the friction coefficient decreased to ~ 0.4. The wear resistance also increased by more than an order of magnitude. Wang et al. [14] modified the surface of pure Fe by implanting different doses of Ta. Their research showed that Ta ion implantation was an effective method to improve the corrosion behavior and cell compatibility of pure iron, so that it can be used for biomedical applications. Chen et al. [15] used Rutherford backscattering spectroscopy (RBS) and transmission electron microscopy (TEM) to study the effects of different implantation temperatures, implantation doses, and annealing temperatures on the formation of surface nitrided layers in pure Fe by N ion implantation, revealing that the stability of nitride phase formed in pure Fe after traditional N ion implantation is independent of whether annealing is performed during ion implantation. ~~In addition to metallic materials, ion implantation for semiconductor materials has also been extensively studied, such as surface modification of semiconductor materials by ion implantation to improve their machinability.~~

It is worth mentioning that numerous studies focus on ion (beam) sputtering and irradiation, as well as plasma etching of surfaces which is similar to ion implantation, but employ different energies for ions [16-20]. They discussed the surface morphology, roughness, nanopatterns, and chemical composition of the samples through

experiments and characterization, including the dependence of these physical characteristics and chemical composition on the ion beam parameters. Overall, achieving a more ideal surface is their goal. However, they are not clear about the mechanism of atomic-scale surface morphology evolution under ion sputtering and irradiation. The addition of this part of the research will make their work extremely challenging and interesting.

All the aforementioned studies show that ion implantation is a very promising surface modification technology in the advanced manufacturing process of materials. Evidently, exploring the effect and characterizing ion implantation has also been a widespread topic in research studies, but there is no theoretical basis for the setting of initial process parameters. Even though some characterization equipment can provide insights into nanoscale phenomena, it is very challenging to have a full image of the effect of the ion implantation on materials. This leads to not be able to provide a solid explanation on the underlying mechanism of the resulting modification. Even so, it is common knowledge that ion implantation experiments and the subsequent characterization experiments at the nanoscale are extremely expensive and time-consuming. Therefore, it would be preferable to have tools to calculate the optimal process parameters and the nanoscopic modification mechanisms of the process.

MD simulation is a particularly effective theoretical method for discrete atom modeling [21]. This method has the capacity to explain the dynamic evolution behavior of atoms via their interaction [22], thus to reproduce the ion implantation process and reveal the underlying modification mechanism. Subsequently, MD simulation is widely used in picosecond and nano-space-time scales to study ion implantation. Kang et al. [21] studied the surface morphology, projection range, defects, RDF, and residual stress after Cu2 + assisted H + co-implantation into single crystal 4H-SiC with the use of MD simulation and verified the reliability of the method using experiments. Evidently, any change of surface morphology and generation of defects after ion implantation affect the mechanical properties of the material. Wu et al. [23] established an ion implantation and nanoindentation MD model to discuss the effects of different implantation energies, doses, and angles on the defect evolution and the mechanical properties of single crystal

3C-SiC. Their results show that ion implantation reduces the hardness and the elastic modulus of single crystal 3C-SiC, and 7.51292 × 10^{13} ions/cm^2 and 500 eV are the best for the implantation dose and energy respectively. Xiao et al. [24] studied the recovery mechanism of Ga focused ion beam on the surface damage of monocrystalline silicon and subsequent annealing by MD simulation. Although they discussed the effect of implantation energy, the implantation energy is still not enough for both ion implantation and FIB milling in MD simulation.

Additionally, MD simulation of ion implantation assisted ultra-precision machining of hard and brittle materials as for example semiconductors, attracting much attention in recent years [25-30]. These studies showcase that ion implantation can significantly reduce the cutting force in nano-cutting process and prolong the service life of a tool. Different ion implantation parameters have different degrees of improvement in cutting machinability. These studies also reveal the damage evolution and material removal mechanism from different angles at the nanoscale level.

In terms of metallic materials, Lebeda et al. [31] quantified the depth distribution of low-energy N ion implantation into single crystal α-Ti by MD and TRIM simulation, and managed to reveal the influence of channel effect on the depth distribution, which is of great significance for the controllable modification of the modified layer. Zhang et al. [32] used MD simulation to study the effect of point defects, which are generated by particle bombardment, on the deformation behavior and the phase transition of body-centered cubic (bcc) iron under tensile load, without providing an explanation of how point defects affect its deformation behavior and phase transition. In addition, the ion implantation process is also accompanied by the occurrence of phase transitions, an important point that has not yet been considered. Jiang et al. [33] constructed a single crystal iron ion implantation model with defects, aiming to study the effect of Cr ion implantation on the hardness of single crystal iron with defects. Through nanoindentation MD simulation, it was found that Cr ion implantation improved the nano-hardness of single crystal iron with defects. In addition, they provided a brief discussion on the nanostructure evolution after ion implantation, but no deep-understanding could be reached. Taghinejad et al. [34] described the surface interaction

and sputtering process of Ar ion implanted single crystal iron in detail by MD method, and accurately calculated the sputtering yield under different implantation parameters. It was found that when the incident angle was 37 degrees, the sputtering yield was the highest, and the surface binding energy and threshold energy were the lowest. Kim et al. [35] studied the sputtering phenomenon caused by low-energy Ar ion bombardment of Fe by MD simulation. It was found that the sputtering yield predicted by MD simulation was in good agreement with the experimental value. By analyzing the calculation results, the threshold energy of sputtering, the kinetic energy distribution of sputtering atoms, and their depth origin were obtained. Peng et al. [36] reported a new mechanism for the formation of <100> interstitial dislocation loops in bcc iron through supersonic shockwave, using a fairly large-scale MD model they established. Granberg et al. [37, 38] used MD to conduct cascade simulation to study the damage behavior of tungsten under high-dose irradiation, focusing on the evolution of dislocation loops.

However, the above-mentioned studies of ion implantation MD simulation are mainly focused on hard and brittle ceramic materials, especially semiconductor materials. For pure metallic materials, more reports focus on ion irradiation and sputtering, and to our knowledge there is scarce research in literature that focuses on the MD simulation of the ion implantation of single crystal iron, a fact that leads to a lack of understanding of the nanoscale modification mechanism of ion implantation single crystal iron. In addition, the MD simulation of ion implantation in semiconductor materials is limited to relatively low implantation energy, which often ignores some noteworthy phenomena and unique insights brought by large implantation energy. Subsequently, this lack of research is affecting ones understanding of the mechanical properties of materials, as well as the generation and evolution mechanisms of dislocations during the ion implantation process.

The research object of the current paper is Cr ion implantation into single crystal iron. Using MD simulations, this work aims to study the ion implantation process and the nanoscale modification mechanism. Iron-based alloys are mainly composed of bcc iron or α-Fe, therefore, in this MD simulation process the influence of alloying elements is not studied. This paper focuses on the effects of Cr ion implantation energy and dose

on surface morphology, ion distribution, vacancies and interstitials, sputtering yield, lattice structure, dislocation evolution, and residual stress. These are necessary to gain an understanding on the ion implantation process and surface modification mechanism of iron-based alloys at the atomic scale. All MD simulations are performed using lammps [39], and the data obtained are visualized with OVITO software [40].

2. Simulation method

2.1. MD simulation model

The MD simulation model can be seen in Fig. 1, and consists of Cr ions and bcc single crystal iron sample. The Cr ions are directly above the single crystal iron at a distance of 30 Å from the upper surface. To effectively reduce the channel effect during the implantation process, the angle between the velocity direction of the implantation ions and the negative direction of the Z-axis is 7° [41]. To ensure the integrity of the boundary atoms, the size of the bcc single crystal iron sample is designed to be 40a × 50a × 60a (lattice constant a = 2.86Å), containing 240000 atoms. The sample is divided into three parts: boundary layer, thermostatic layer, and Newtonian layer. The atoms in the boundary layer are fixed to prevent the sample from moving during ion implantation, with a height of 3 Å. The thermostatic layer is useful for heat exchange and dissipation between the system and the external environment, with a height of 36 Å. To maintain the stability of the system, it is reasonable to set up a sufficiently thick thermostatic layer [42]. The Newtonian layer is used to simulate the actual ion implantation process and its dynamic response. The atoms of the thermostatic layer and the Newtonian layer follow Newton ‘s second law. The three directions of the sample are x-[100], y-[010], and z-[001]. To approximately describe the related properties of the macroscopic system under the finite particle system, the x and y directions are set as periodic boundary conditions. The non-periodic boundary conditions are applied in the z direction, and the particles leaving the simulation box from the top or bottom are considered to be lost and are removed from the system.

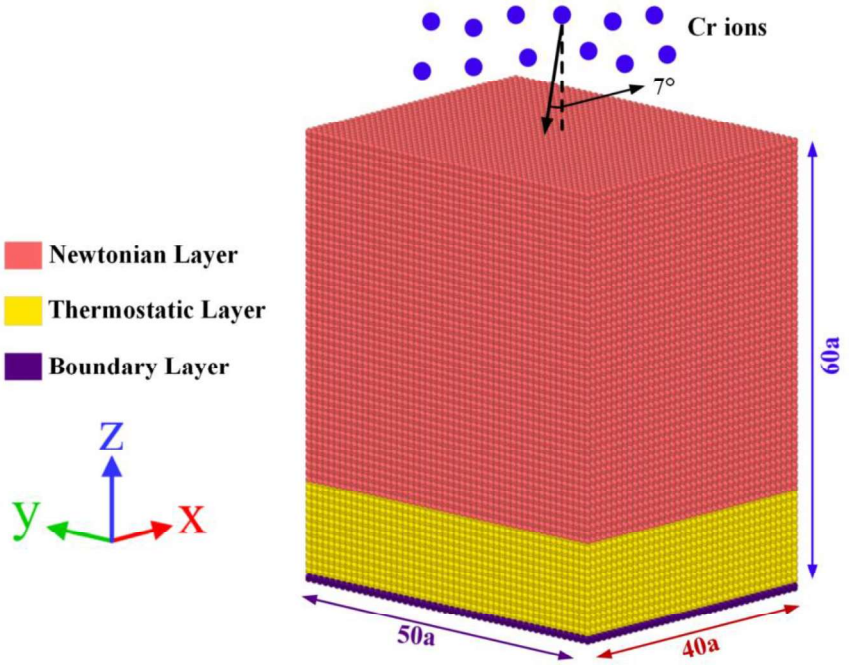

Fig. 1. MD simulation model, consisting of a Newtonian (Red), Thermostatic (Yellow), and a Boundary (Magenda) Layer.

2.2. Simulation parameter design

Before simulation, the energy of the system is minimized by the conjugate gradient algorithm to avoid any possible atomic overlap effect. The simulation itself can be divided into three stages, namely relaxation, ion implantation, and annealing. At the relaxation stage, the NVT ensemble is used to run 30,000 time steps to balance the system at 300 K, and the time step is set to 1 fs [43]. In the ion implantation stage, the system is controlled by the NVE ensemble to ensure that the total energy of the system remains unchanged during the collision process. The temperature of the thermostatic atoms is limitedly regulated by the Berendsen thermostat [44]. At the simulated implantation process, Cr ions are randomly generated at 3 nm from the (001) upper surface of the sample, and its position obeys a Gaussian distribution with a standard deviation of 2.5 nm [45]. One Cr ion is implanted at a time, and the next ion is implanted after an interval of 20,000 time steps, which is enough to dissipate kinetic energy and reduce the cumulative effect of temperature [46]. To improve the simulation accuracy and the possibility of cascading collisions, an adaptive time step is used so as to ensure

that the distance of particles, which are moving within a single time step, does not exceed 0.05a [47]. At the annealing stage, the time step is reset to 1 fs and the system temperature is reduced to 300 K, by running 200 ps in the NVE ensemble. During the whole simulation process, the velocity-Verlet algorithm is selected in order to integrate the motion equation, to obtain the atomic position, as well as the velocity vector [48].

Referring to the ranges provided by studies in literature and considering the differences of the models [24, 28, 31], five groups of different implantation energies and doses are selected for simulation. These are 1 keV, 1.5 keV, 2 keV, 2.5 keV, 3 keV and 3.06×10^{13} ions/cm^2, 4.58×10^{13} ions/cm^2, 6.11×10^{13} ions/cm^2, 7.64×10^{13} ions/cm^2, 9.17×10^{13} ions/cm^2, respectively. When discussing the influence of implantation energy, the implantation dose corresponding to these five groups of different implantation energies is 6.11×10^{13} ions/cm^2; when discussing the influence of the implantation dose, the energy corresponding to different implantation doses is 1 keV.

It is common knowledge in literature that the choice of potential function not only affects the efficiency and sustainability of the calculation, but also is crucial for the accuracy of the simulation results[21]. In this study, the embedded atom method (EAM) form of the interatomic potential function proposed by Mendelev et al. [49], is used to describe the interaction and the short-range collisions between Fe-Fe. According to previous studies, this potential function is widely used to study the particle bombardment of single crystal iron [32, 50, 51], which can indirectly prove its reliability and consistency. The interaction between Fe and Cr is described by the Tersoff / ZBL potential [52], which is a combination of the Tersoff potential [53] and the ZBL potential [54]. It contributes to the accurate expression of the stopping and short-range interactions of incident ions [55]. Since Cr ions are in discrete form, using solely other potential functions to describe the interaction between Cr-Cr has a negligible impact on the simulation accuracy. Therefore, the same Tersoff/ZBL potential is used in this case. The main parameters of the simulation are shown in Table 1.

Table 1. MD simulation parameters

Condition	Parameters
Work material	Bcc Fe
Model size (Å)	114.4 × 143 × 171.6
Total number of atoms	240000
Initial temperature (K)	300
Potential function	EAM, Tersoff/ZBL
Ensemble of implantation	NVE
Boundary conditions	P P F
Thermostatic setup	Berendsen
Timestep of implantation	Adaptive timestep
Timestep of annealing(fs)	1
Incident angle(°)	7
Incident height	3 nm from the upper surface
Implantation energy(keV)	1.0, 1.5, 2.0, 2.5, 3.0
Implantation dose (ions/cm^2)	3.06×10^{13}, 4.58×10^{13}, 6.11×10^{13}, 7.64×10^{13}, 9.17×10^{13}

2.3. Model verification

In order to verify the effectiveness of the established ion implantation MD model and the rationality of its parameter design, Monte Carlo simulation of ion implantation was performed using SRIM software [56]. It was decided that the same implantation energy and angle were set for both MD and Monte Carlo simulations. 100 ions are implanted in the MD simulation and 100,000 ions are implanted in the Monte Carlo simulation, since for the Monte Carlo simulation the more ions are implanted, the more accurate the results will be.

Fig. 2 shows the distribution of the number of ions against depth in MD and Monte Carlo simulations, for implantation energy of 1 keV and the incident angle of 7°. Since the underlying calculation principle and the number of implanted ions of the two

simulation methods are different, only the consistency and trend of the distributions is considered in this work, following the example of other published work [57]. It can be clearly seen from Fig. 2 that the distribution of ions in a single crystal iron that are obtained by the two simulations appears to be similar, and that the peak concentration and variation trends are approximately the same. The difference lies in the fact that for the MD simulation results, a number of implanted ions are distributed deeper. This can be attributed to the unavoidable channel effect, in combination with the influence of atomic vibration [45]. The results of the SRIM software simulation undoubtedly show that Cr ions follow a Gaussian distribution in single crystal iron. For this reason, Gaussian fitting was performed on the results that were obtained from the MD simulation. The R square value after iteration reached 0.858. The fitting curve is depicted in Fig. 2. Evidently, the fitting result is quite satisfactory, showcasing that the ion distribution, which is simulated with the use of the established MD model, also follows a Gaussian distribution. This phenomenon is consistent with numerous results of ion implantation experiments in literature [9, 58, 59]. Overall, these results and analysis, strongly prove the effectiveness and rationality of the MD.

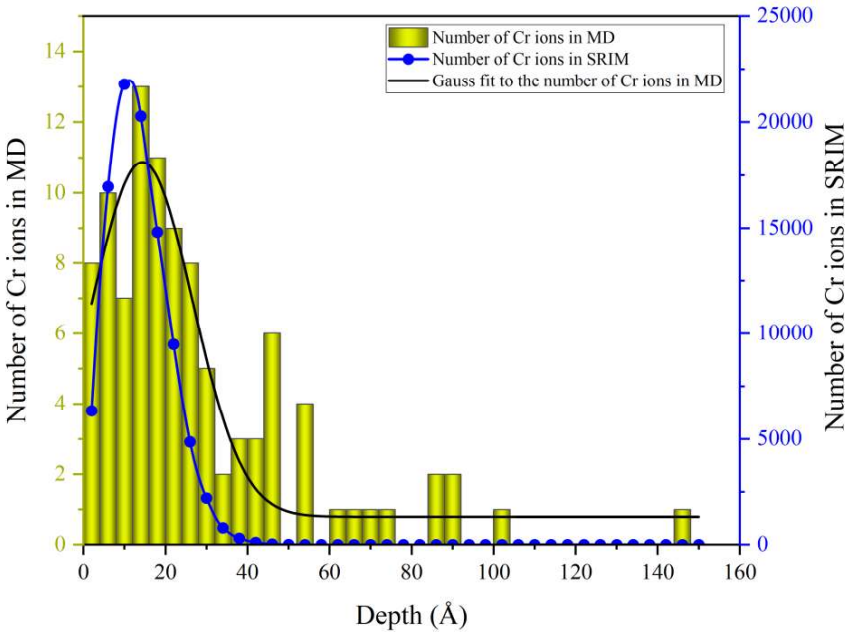

Fig. 2. Graph showing the variation of the number of Cr ions to their depth in a single crystal iron for both MD and Monte Carlo simulations for implantation energy of 1 keV

and the incident angle of 7 °. Notice the Gaussian fit to the number of Cr ions in MD plot, as compared to the rest.

3. Results and discussion

3.1. Surface morphology

During the ion implantation process, ions first pass through the sample surface and then move to the subsurface. Therefore, the change in the sample surface is taken as the entry point in this research. The surface morphology under different implantation energies and doses was observed via coloring the height values of the atomic centers (see Fig. 3). Due to ion bombardment, bulges and pits appear on the initially flat surface. According to literature, this is caused by the sputtering of atoms on the sample surface during the ion bombardment process, and the subsequent migration of free atoms after the lattice is destroyed [60]. By comparing the surface morphology under different energy and dose, it can be found that with the increase of energy, the area of bulges and pits becomes larger and larger. The increase of dose though, does not appear to have any significant effect to the area of bulges and pits, showcasing the dominance of the influence of ion implantation energy on the surface morphology, a fact also consistent with our consistent cognition. In parallel, the sputtering effect becomes more obvious with the increase of the implantation energy. In Fig. 3(d), it can be seen that when the implantation energy is 3 keV, the depth of the pit caused by the sputtering reaches 15.6 Å (while the initial surface height is 171.6 Å).

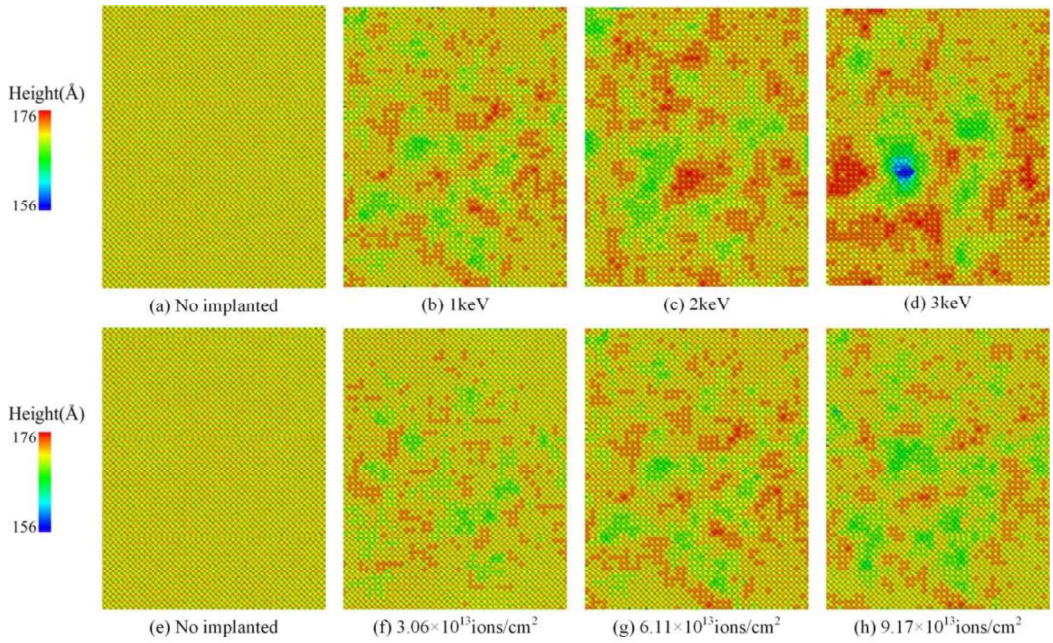

Fig. 3. Surface morphology of bcc Fe with Cr ion implantation under different energies (b-d) and doses (f-h). (a) Reference sample with no implantation. (b) Sample after 1 KeV implantation. (c) Sample after 2 KeV implantation. (d) Sample after 3 KeV implantation. (e) Reference sample with no implantation. (f) Sample after 3.06×10^{13} ions/cm^2 implantation. (g) Sample after 6.11×10^{13} ions/cm^2 implantation. (h) Sample after 9.17×10^{13} ions/cm^2 implantation. Note that (b)-(d) correspond to 6.11×10^{13} ions/cm^2 and (f)-(h) correspond to 1 keV.

Surface roughness is an important in order to evaluate the surface integrity of a sample after ion implantation. The discrete form of two-dimensional surface root mean square roughness (Sq) is a reliable statistical tool that can be employed for quantitative analysis of the surface roughness changes after ion implantation. The calculation formula is as follows [24]:

$$Sq = \sqrt{\frac{1}{mn}\sum_{i}^{m}\sum_{j}^{n}\left(H_{ij} - \overline{H}\right)^2} \tag{1}$$

Where m and n are the number of rows and columns of the surface height matrix, H_{ij} is the surface height value of row i and column j, and $\overline{H}$ is the average surface height value.

Using the calculations of the variation of root mean square roughness with implantation dose and energy we obtain a graph that can be seen in Fig. 4. There, one can see that the root mean square roughness of the surface after implantation increases with the implantation energy. The root mean square roughness under different energies shows a fluctuating upward trend when implantation dose increases. An analogous relationship for implantation energy and fluctuations, as well as variation range, showing that the main process parameter for surface roughness of a sample is the implantation energy.

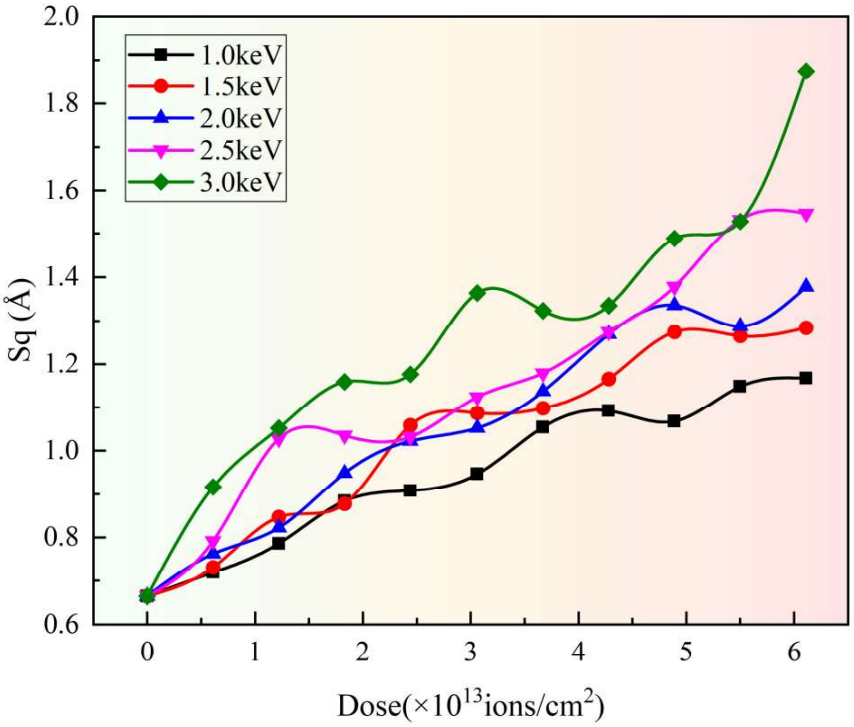

Fig. 4. Variation of root mean square roughness against dose using different energies (1.5, 2.0, 2.5, 3.0 keV) in Cr ion implantation of bcc Fe.

3.2. Ion distribution

Ion distribution is a key dynamic response index of the ion implantation process parameters. Characterizing its distribution in a sample can provide important feedback for the formulation of process parameters. In experiments, the Rietveld method in the FullProf program can be used to analyze neutron diffraction spectra to obtain ion distribution [61], while in MD simulations, the atomic coordinates of Cr in the single

crystal iron system can be obtained through computation. Fig. 5 shows the three-dimensional ion distribution at different energies and doses after annealing. It can be seen from Fig. 5 (a)-(e) that the implantation energy can significantly change the implantation depth of ions. At higher implantation energies the ions reach deeper inside the sample. Another notable observed phenomenon is that the lateral and longitudinal straggle of the implanted ions increase analogously with energy. These phenomena can be attributed to the fact that an increase in implantation energy can cause more surface atoms to sputter and thus, more serious collision cascades appear. As the implantation progresses, sputtering and collision cascades intensify, resulting in part of the ions to be implanted into the subsurface of the sample without overcoming the surface potential barrier, which means that more implanted ions will lose all their energy at a deeper depth before they stop. The above observed behavior was not found in the three-dimensional ion distribution at different doses (Fig. 5(f)-(j)). The maximum implantation depth of a single ion remains unaffected by any increase of ion dose, as it has little effect on the implantation depth. The main observed influencing factor is the implantation energy, i.e. the initial kinetic energy of the ion. However, when the dose increases more than a certain point, the cumulative effect of sputtering and collision cascades is also expected to increase the maximum depth of ion implantation [30]. The ions at different implantation doses are typically concentrated in the modified layer of about 2 nm. Increases of dose increases the ion concentration at the same depth, which is reflected in the increase in the distribution of ions. Subsequently, the average implantation depth at different energies and doses after annealing was calculated, and the results are shown in Fig. 6. With the increase of the implantation energy, the average depth of ions also increases, but when the energy increases to 2.5 keV the average depth does not change significantly. It can be speculated that in this simulation system, the threshold energy affecting the ion implantation depth is about 2.5 keV. It can be seen from Fig. 6(b) that the increase in dose hardly changes the average depth of the ions. It should be noted that at the minimum dose the implanted ions are more dispersed (Fig. 5(f)), thus they obtain there a maximum average value, without this affecting the above conclusion.

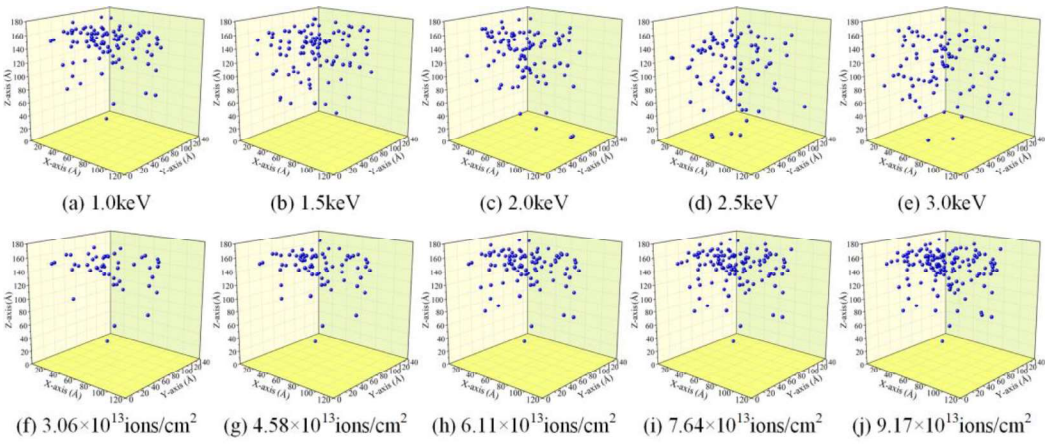

Fig. 5. Three-dimensional diagram of ion distribution during Cr ion implantation in bcc Fe. (a) Sample after 1.0 KeV implantation. (b) Sample after 1.5 KeV implantation. (c) Sample after 2.0 KeV implantation. (d) Sample after 2.5 KeV implantation. (e) Sample after 3.0 KeV implantation. (f) Sample after 3.06 × 10^{13} ions/cm^2 implantation. (g) Sample after 4.58 × 10^{13} ions/cm^2 implantation. (h) Sample after 6.11 × 10^{13} ions/cm^2 implantation. (i) Sample after 7.64 × 10^{13} ions/cm^2 implantation. (j) Sample after 9.17 × 10^{13} ions/cm^2 implantation. Note that (a)-(e) correspond to 6.11 × 10^{13} ions/cm^2 and (f)-(j) correspond to 1 keV.

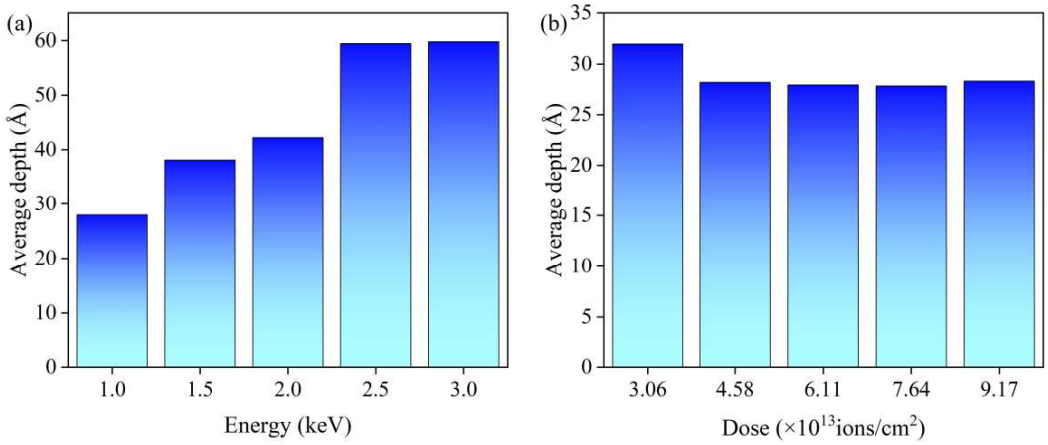

Fig. 6. Average depth of implanted ions Vs Energy (a) and Dose (b) for Cr ion implantation in bcc Fe. Note the dependency of depth from energy change, and the fact that Dose does not seem to significantly influence the average depth.

3.3. Surface/subsurface damage analysis

During the ion implantation process, high-energy ions collide with the sample's atoms and generate displacement cascades. Therefore, the atoms that are arranged in an orderly manner around the ion trajectory become disordered, resulting in lattice damage and defects. The atom that is displaced during the collision itself can occupy an interstitial or a substitutional site, leaving a vacancy at its original site. Additionally, the implanted ions can stay in the interstitial sites or stay in the vacancies and become substitutional impurities. Therefore, ion implantation forms three types of point defects in the solid: vacancies, interstitial atoms, and substitutional impurity atoms. Their presence increases the degree of lattice disorder and lattice distortion inside the sample. These internal defects can increase the lattice stress and hinder the dislocation movement, thereby improving the mechanical properties of the material [62, 63]. Additionally, different forms of defects also affect the physical properties of the material [64]. Wigner-Seitz (WS) defect analysis method can be used to quantitatively describe the point defects that are produced by ion implantation in perfect crystals [65]. Fig. 7(a)-(c) shows the variation trend of vacancies and interstitials in single crystal iron. It can be seen that the variation trend of the number of vacancies and interstitial atoms with dose shows excellent consistency. With the increase of implantation dose, vacancies and interstitial atoms accumulate continuously. Increasing implantation energy results in the creation of more vacancies and interstitial atoms. In fact, with this increase of implantation dose, the increment of vacancies and interstitial atoms is gradually decreasing. When the implantation dose reaches a certain value, the number of vacancies and interstitial atoms gradually stabilizes. The named certain dose and the stable value depend on the implantation energy, which is consistent with the research results of Tong et al. [66]. For implantation energy of 1 keV, obvious saturation occurs when the dose reaches approximately 6.11×10^{13} ions/cm^2, as shown in Fig. 7(c). The degree of subsurface damage is close to the maximum at this time, and almost all the atoms in the modified layer are in a disordered state. After reaching the saturation dose, the number of vacancies continues to increase due to the sputtering that is caused by ion implantation, so the saturation phenomenon of vacancies will lag behind that of

interstitial atoms. Interestingly, in Fig. 7(a) and (b), one can see that when the implantation energy is 3keV, multiple "spikes" appear on the curve, showing that the number of vacancies and interstitial atoms abruptly increases significantly, and then drops back to the previous state. A similar behavior was documented in the study of Zhao et al. [67]. To explain this phenomenon, the time step of the dump is reduced to determine more details of the vacancy and interstitial atoms. The displacement vectors module in the OVITO software is used to analyze the atomic displacement at the time of the "spike" and export the snapshot. Two completely different atomic displacement snapshots are shown in Fig. 7(e)-(f). Almost all the interstitial atoms in Fig. 7(e) have a very large displacement, and the displacement direction shows a high degree of disorder. Contrarily, neatly arranged interstitial atoms are seen in Fig. 7(f), with interstitial atoms that have small displacements and the displacement directions showing excellent consistency. The "spike" behavior can therefore be explained by the following two factors. i. When the implantation energy reaches 3keV, ion implantation causes a high-density collision cascade of lattice atoms, and the atoms participating in the collision undergo large-scale displacement (Fig. 7(e)), causing local melting of the collision body, and resulting in obvious thermal spike effects. Increase in energy, leads to increase in the likelihood of occurrence of this thermal spike. This thermal spike behavior lead to a sudden and substantial increase in vacancies and interstitial atoms, and the "spike" appears. The subsequent relaxation process causes recrystallization and the "spike" disappears, which is consistent with the results documented by Mihai et al. [68]. ii. Temperature-induced lattice thermal vibrations and the rearrangement of atoms, in an effort to seek a more stable energy minimum, are likely responsible for generating large-scale ordered arrangements of vacancies and interstitial atoms [69]. Fig. 7(d) shows the variation trend of sputtering yield with the implantation dose under different implantation energies. It can be clearly seen that the initial sputtering yield is very large, and gradually decreases to a stable value with the increase of dose. This behavior can also be observed in previous experiments and simulations [24, 70-72]. When the implantation dose is lower than 1.53×10^{13} ions/cm^2, the curve fluctuates violently. When the dose reaches about 3.06×10^{13} ions/cm^2, the violent fluctuations disappear,

which is consistent with the research data of Gnaser [73]. It is easy to comprehend that at the initial stage of ion implantation the perfect surface begins to be damaged, and most of the sputtering atoms come from the top-layer atoms [74]. At that time the sputtering yield is large and the fluctuations are violent. During the ion implantation process, the surface atoms that are removed by sputtering cause pits to appear on the surface of the sample, thus the surface morphology changes significantly, resulting in the decrease in sputtering yield. Eventually, the surface damage gradually accumulates to saturation, and the sputtering yield also reaches a saturation value. Previous studies have shown that the sputtering yield obtained by MD simulation is higher than the experimental value, which is attributed to the change of surface structure at the atomic scale [75]. Furthermore, the subtle relationship between the thermal spike behavior and the sputtering yield was also noted. When the thermal spike behavior occurs, the sputtering yield suddenly increases, while the appearance of the thermal spike behavior also contributes to the violent fluctuation of the sputtering yield, which explains why when the implantation dose is greater than 3.06×10^{13} ions/cm^2, the sputtering yield of the implantation energy of 3 keV still presents jagged fluctuation.

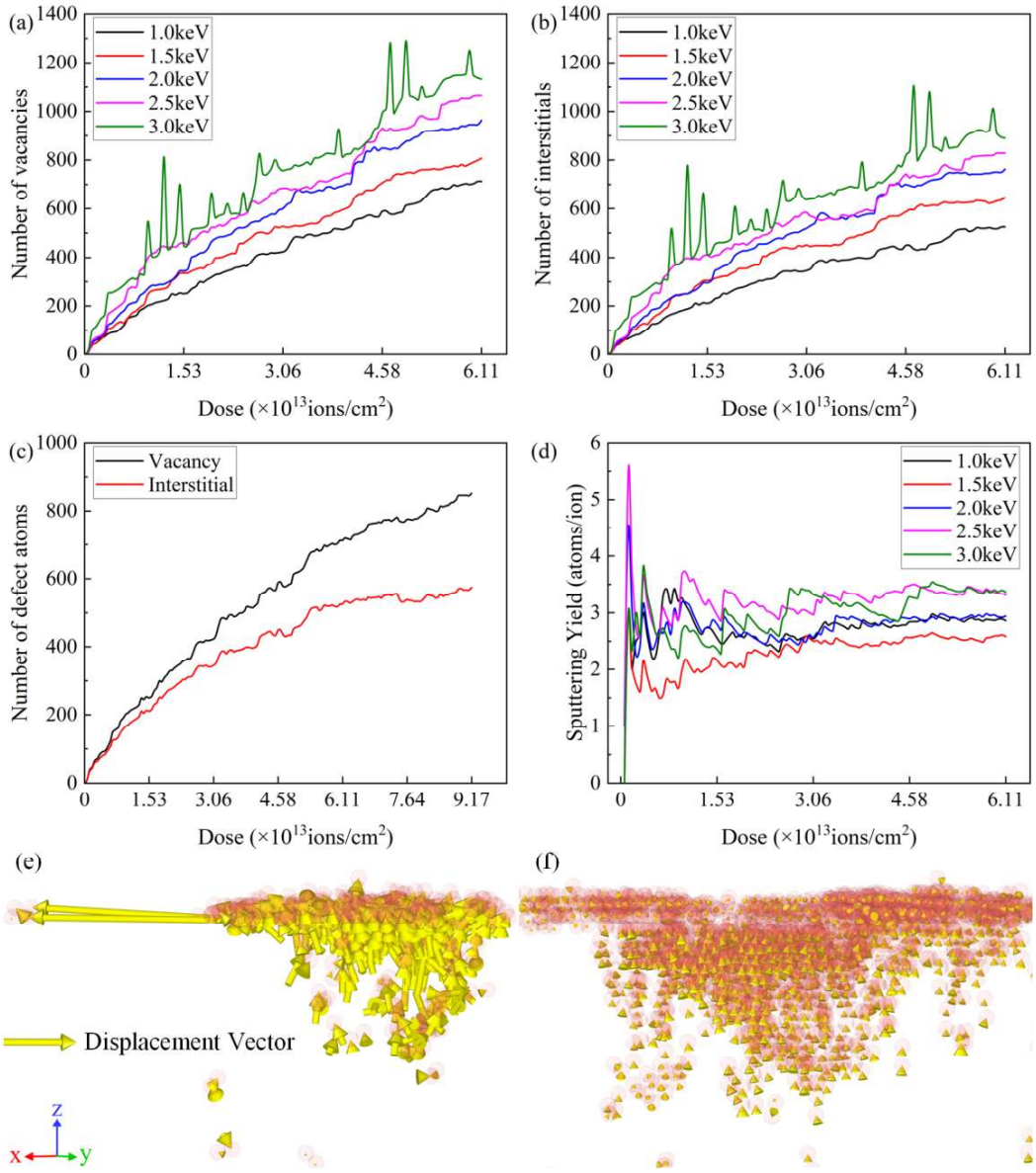

Fig. 7. (a)-(c) Graph of the number of vacancies and interstitials Vs dose for different energies. These graphs showcase the variation trend of vacancies and interstitials. Note that (c) corresponds to an energy of 1 keV. (d) Graph of the sputtering yield versus dose for different energies, showcasing the variation trend of sputtering yield. (e)-(f) Snapshots of two completely different atomic displacement at the moment when the "spike" appears. The atomic displacement is determined by the atomic position of the two adjacent frames. For clarity, the perfect lattice is removed and only the interstitial atoms are retained, while the interstitial atoms are set to be translucent.

Previous studies have shown that the formation of amorphous structure and the transformation of phase structure can significantly improve the hardness of metallic materials [76, 77]. CNA analysis was used to find the transformation of crystal structure during ion implantation. Fig. 8 shows the distribution of amorphous structure under different energies and doses. It appears that the amorphous structure accumulates with the increase of the implanted ions. Energy increase results in the volume of the amorphous region to become significantly larger, which leads to the conclusion that the lattice damage is more serious. By comparing Fig. 5, it can be found that the amorphous structure is generated around the Cr ion implantation trajectory, and its distribution characteristics can be considered consistent with the distribution characteristics of the implanted ions. Distinctively, the collision cascade results in difference in depth and breadth of the distribution of the amorphous structure. These amorphous structures exist in the form of clusters, and high-density amorphous clusters are observed in the modified region. The curve describing the variation of the number of amorphous atoms is shown in Fig. 9(a). Evidently, an increase in the energy of the implantation generates a larger amount of amorphous atoms. In the early stage of ion implantation, the number of the generated amorphous atoms shows a linear relationship with the implantation dose. When the dose reaches 1.53×10^{13} ions/cm^2, the number of amorphous atoms gradually increases until the saturation value, a value that depends on the implantation energy. Apparently, when the lattice damage reaches its saturation, the increase of energy will no longer influence the saturation value of the atoms. When the energy reaches 2 keV, which is considered as a critical value, the number of amorphous atoms begins to fluctuate sharply near the saturation value at a dose of approximately 3.06×10^{13} ions/cm^2. When the implantation energy is high, due to the thermal spike effect and the cumulative effect of temperature, self-annealing and recrystallization occur. However, the transformation between crystal structures becomes easier, which leads to violent fluctuations. Fig. 9(b) shows the cumulative number of typical phase structures FCC and HCP from the start to the end of ion implantation, as well as the average number of other structures during the saturation period (dose greater than 5.50×10^{13} ions/cm^2) as a function of the implantation energy. It can be found that the phase

transformation caused by ion implantation is mainly other structures. The larger the implantation energy, the more serious the phase transformation. Before 2.0 keV, the average number of other structures increases significantly during the saturation period, while the cumulative number of FCC and HCP structures had a minor increase. Higher than 2.0 keV, there was a minor change for the average number of other structures, whereas the cumulative number of FCC structure manifested a step-like increase. This behavior supports the above speculation, while simultaneously indicating that the saturation energy for lattice damage is approximately 2.0 keV.

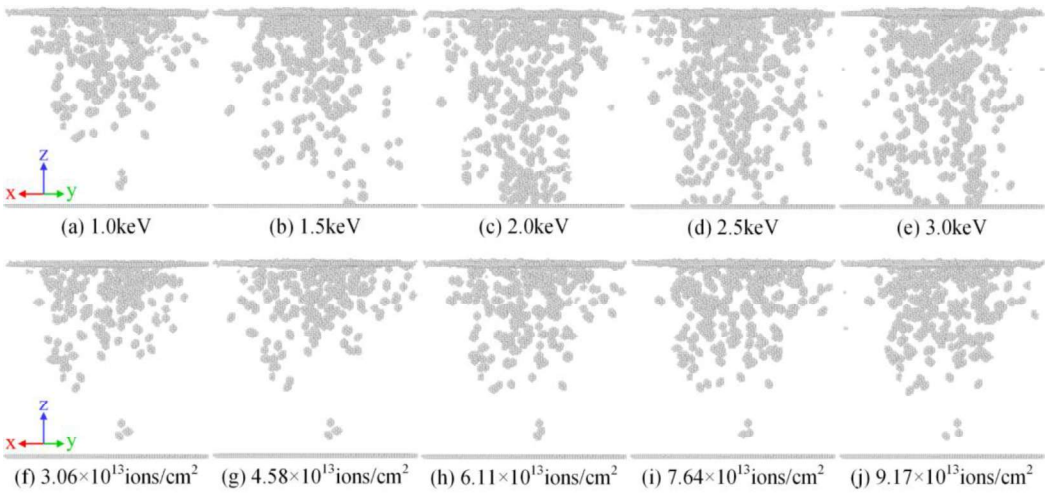

Fig. 8. The distribution of amorphous structure in the bcc Fe sample after Cr ion implantation. For reasons of clarity, the perfect crystal structure has been deleted. (a)-(e) Correspond to the implantation energies of 1.0 keV, 1.5 keV, 2.0 keV, 2.5 keV and 3.0 keV, respectively, and the implantation dose is 6.11×10^{13} ions/cm^2. (f)-(j) Correspond to the implantation doses of 3.06×10^{13} ions/cm^2, 4.58×10^{13} ions/cm^2, 6.11×10^{13} ions/cm^2, 7.64×10^{13} ions/cm^2 and 9.17×10^{13} ions/cm^2, respectively, and the implantation energy is 1.0 keV.

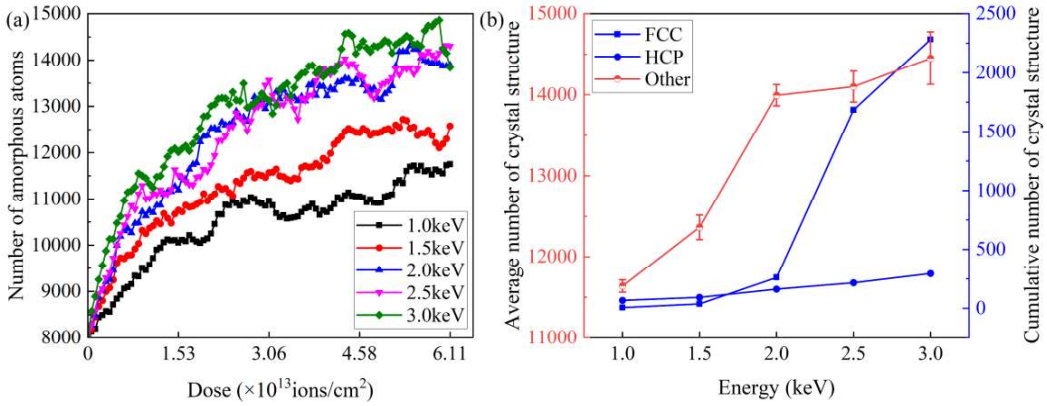

Fig. 9. (a) The variation of the number of amorphous atoms with the implantation dose at different energies. (b) The cumulative number of FCC and HCP structures, and the average number of other structures during the saturation period change with the implantation energy, these energies correspond to a dose of 6.11×10^{13} ions/cm^2.

3.4. Dislocation analysis

Dislocation is one of the crucial defects affecting the mechanical properties of materials. Experiments prove that dislocations can be generated by ion implantation [78, 79], which makes the realization of dislocation strengthening possible. However, there is no report in literature that shows this using simulation. Based on the understanding of previous experimental and simulation results, the common understanding is that dislocations are likely to be generated inside the sample only when the implantation energy is exceptionally high. To determine whether dislocations were generated in Cr ion implanted single crystal iron, the dislocation extraction algorithm (DXA) in OVITO software was employed, so as to identify dislocations and calculate the dislocation length [80]. The variation of the total dislocation length with the implantation dose under different implantation energies can be seen in Fig. 10(a). Apparently, it appears that dislocations are generated during the ion implantation process, even at lower doses of approximately 1×10^{13} ions/cm^2, but a higher implantation energy results in more dislocations and greater fluctuations in the total dislocation length. As ion implantation continues, the generation and disappearance of dislocations make the variation trend of the curve become more stochastic. When the

energy is 1.5 keV and 2 keV, the generated dislocations disappear immediately in the subsequent implantation stage and do not reappear. This is attributed to the evolution and stability of dislocations. At 6.11 × 10^{13} ions/cm^2, no dislocations were generated at an implantation energy of 1 keV. Surprisingly, when the ion implantation dose continues to increase until approximately 7.64 × 10^{13} ions/cm^2, dislocations are generated. Analyzing Fig. 10(a) it is important to note that with the increase of implantation energy, dislocations appear to be generated at an earlier stage. Therefore, it can be concluded that the generation of dislocations is not only a function of implantation energy, but also a function of implantation dose. Additionally, since the total dislocation length curves at different energies are staggered, in order to understand the relationship between implantation energy and dislocation length more, the average dislocation length is plotted as a function of the implantation energy at a dose of 6.11 × 10^{13} ions/cm^2 (see Fig. 10(b)). The graph clearly shows that the average dislocation length increases with the augmentation of implantation energy, a behavior which is similar to the variation trend of lattice damage, amorphous structure, and phase transformation.

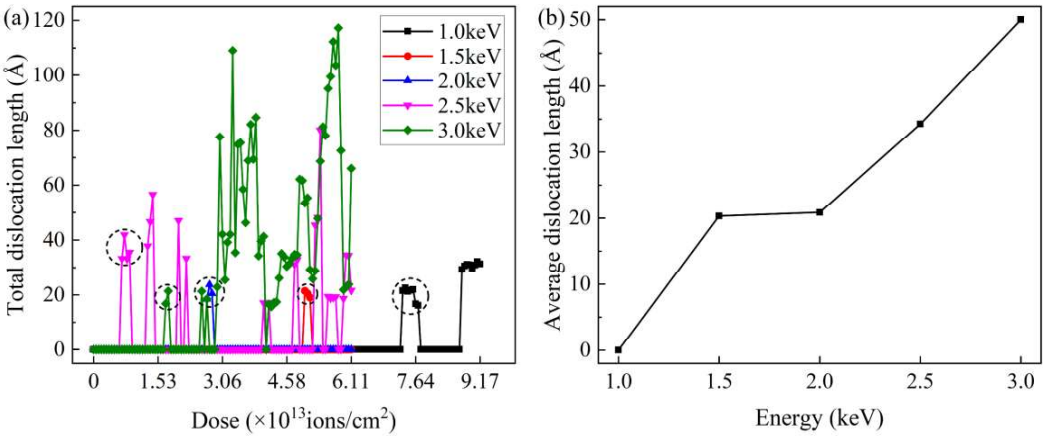

Fig. 10. (a) The variation of total dislocation length with implantation dose under different implantation energies, the dotted circle in the figure is the visual guidance of the dose when the dislocation first appears. (b) The average dislocation length under different implantation energies when the dose is 6.11 × 10^{13} ions/cm^2, which shows the average level of dislocation length under different implantation energies.

Fig. 11 shows the types of dislocations that are formed during the ion implantation process. These dislocations are dislocation loops that are formed due to the aggregation of interstitial atoms and vacancies, which are 1/2<111> interstitial-type dislocation loops (Fig. 11(a)), 1/2<111> vacancy-type dislocation loops (Fig. 11(b)), and <100> vacancy-type dislocation loops (Fig. 11(c)) respectively. Amongst these five named groups of different implantation energies, the generated types of dislocation loops are mainly 1/2<111> interstitial-type dislocation loops, and sporadically 1/2<111> vacancy-type dislocation loops. At energies of 2.5 keV and 3 keV a small number of <100> vacancy-type dislocation loops can also be formed. This is attributed to the fact that 1/2<111> dislocation loops have a lower formation energy than <100> dislocation loops, and the lower the formation energy, the easier it is for dislocation loops to form [81]. Compared with 1/2<111> dislocation loops, <100> dislocation loops are considered to have stronger resistance to dislocation motion.

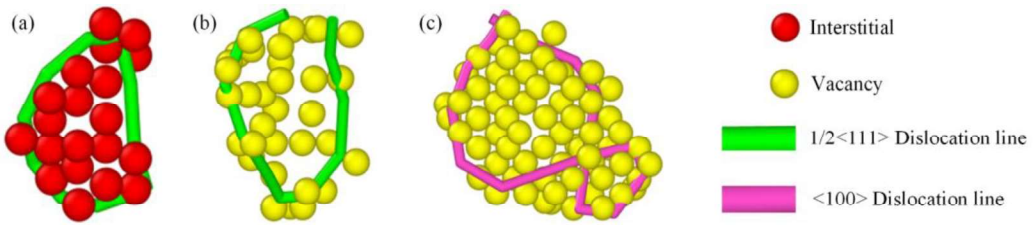

Fig. 11. Types of dislocation loop. (a) 1/2<111> interstitial-type dislocation loop. (b) 1/2<111> vacancy-type dislocation loop. (c) <100> vacancy-type dislocation loop.

To further clarify the specific evolution characteristics of dislocation loops during ion implantation, we acquired typical snapshots of the evolution of dislocation loops under different energies, which can be seen in Fig. 12. Fig. 12(a1)-(a3) show that as ion implantation proceeds, the 1/2<111> dislocation loop gradually slips toward the surface in a direction parallel to the Burgers vector and eventually annihilates. At an implantation dose of 7.64×10^{13} ions/cm^2, the 1/2<111> dislocation loop is positioned as shown in Fig. 12(a1). There, increasing the dose to 7.70×10^{13} ions/cm^2, the dislocation loop slips toward the surface to the position shown in Fig. 12(a2), whereas

during the subsequent equilibrium process, the dislocation loop continues to slip towards the surface, as shown in Fig. 12(a3). When dose reaches 7.76×10^{13} ions/cm^2, the dislocation loop disappears. This is attributed to the fact that the 1/2<111> dislocation loop is highly mobile and can perform an one-dimensional diffusion in a direction parallel to its Burgers vector [82]. This mechanism explains the behavior that is observed in Fig. 10(a), where the curve rises and then drops to zero. Fig. 12(b1)-(b3) show the transformation process from the <100> dislocation loop to the 1/2<111> dislocation loop. After the interaction of two <100> dislocation loops with the same Burgers vector and similar size, initially a larger <100 > dislocation loop is formed, and then a 1/2<111> dislocation loop is generated in the vertical direction. This reduces the proportion of <100> dislocation loops to a certain extent. Differently from Fig. 12(a1)-(a3), one can observe that in Fig. 12(c1)-(c2) two 1/2[11-1] dislocation loops collide with the nearby 1/2[1-11] dislocation loop during the slip along the <111> direction, and begin to react and eventually forming a larger 1/2[11-1] dislocation loop (Fig. 12(c3)). This is a typical behavior, when one loop absorbs another. In addition to annihilation and reaction mechanisms, a dynamic stabilization process of 1/2<111> dislocation loops was also observed. As shown in Fig. 12(d1)-(d3), the length of the 1/2<111> dislocation loop reduces from 31.3 Å to 29.9 Å, but then expands to 33.2 Å. This dynamic stabilization process is the absorption and the dynamic motion of point defects. It is worth to note that the dynamic stabilization of this dislocation loop is not limited to these three moments but persists for a considerable period of time.

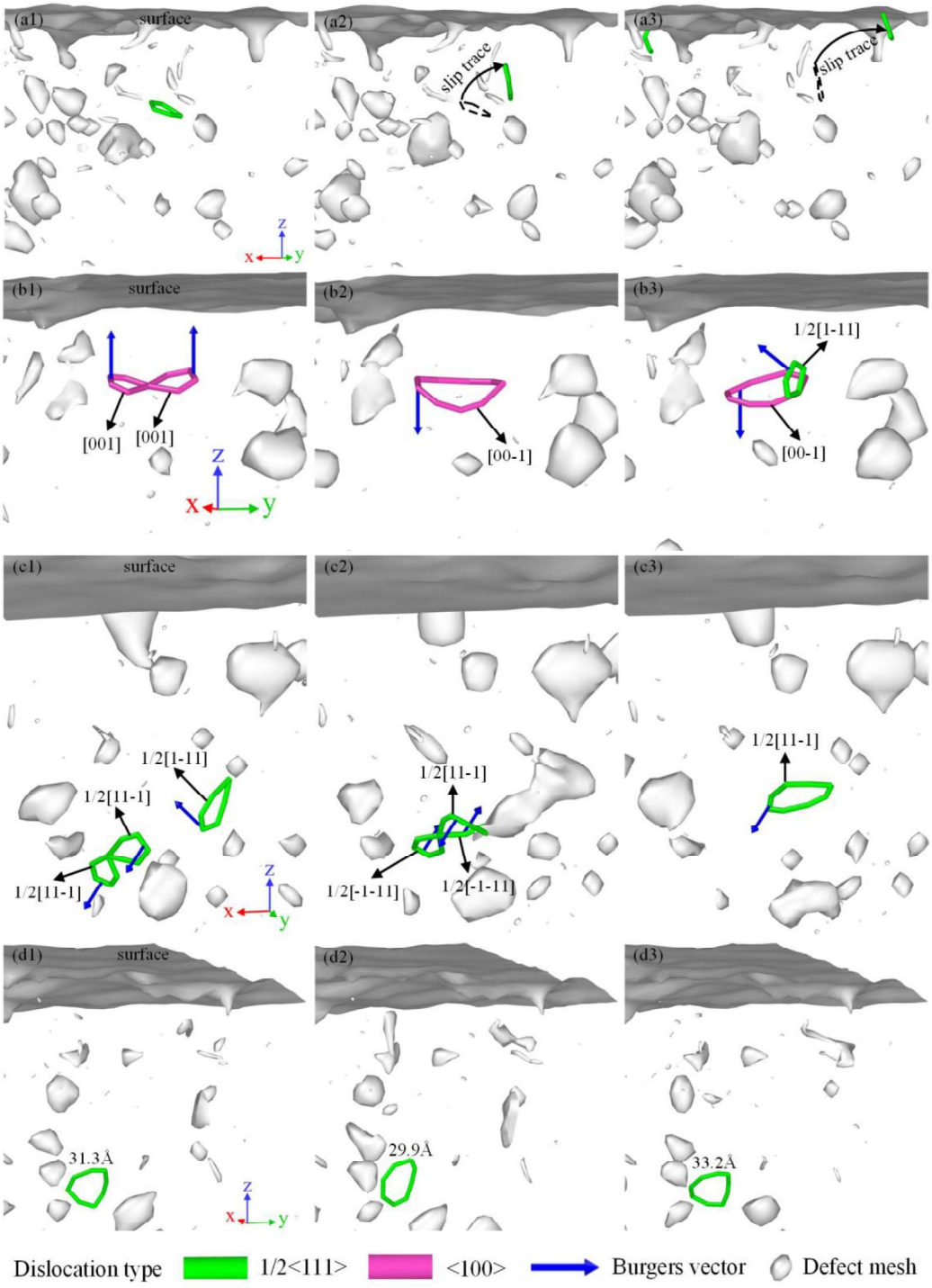

Fig. 12. The evolution process of dislocation loops under different energies. (a) As ion implantation proceeds, the 1/2<111> dislocation loop gradually slips toward the surface in a direction parallel to the Burgers vector and eventually annihilates. (b) The transformation process from the <100> dislocation loop to the 1/2<111> dislocation loop. (c) Two 1/2[11-1] dislocation loops collide with the nearby 1/2[1-11] dislocation

loop during the slip along the <111> direction, and begin to react and eventually forming a larger 1/2[11-1] dislocation loop. (d) The dynamic stabilization process of 1/2<111> dislocation loops. (a)-(d) Correspond to the implantation energies of 1.0 keV, 2.5 keV, 3.0 keV, and 3.0 keV respectively, and the implantation dose is 6.11×10^{13} ions/cm^2.

3.5. Residual stress analysis

Residual stress can significantly affect the performance and service life of a sample workpiece. The distribution and magnitude of residual stress are critical indicators to evaluate the surface integrity of the sample. The lattice distortion, phase transformation, and thermal stress generated during the ion implantation process bring forward the appearance of residual stress to the sample. According to literature [22], the stress components σ_{xx}, σ_{yy}, σ_{zz}, σ_{xy}, σ_{xz} and σ_{yz} for each atom can be calculated using the following equation:

$$\sigma_{ab} = \frac{1}{\Omega}\sum_{i}^{N}\left(m_i v_{ia} \otimes v_{ib} + \frac{1}{2}\sum_{i \neq j} r_{ija} f_{ija}\right) \tag{2}$$

In the analysis of gear fatigue life, it is generally believed that residual stress in the tangential direction has the most significant impact on fatigue life. Therefore, the variations in residual stress in the X-direction of the sample were analyzed. In Fig. 13, a sample exhibits significant residual stress after ion implantation. Specifically, substantial residual tensile stress is observed on the upper and bottom surfaces of the sample, while noticeable residual compressive stress is present in the subsurface, as well as the interior of the sample. For the bottom surface, the existence of a boundary effect results in highly tensile stress in the bottom atomic layers. Simultaneously for the upper surface, the generation of significant residual tensile stress can be attributed to the elastic recovery before localized plastic deformation, combined with the substantial thermal effect that is induced by the ion implantation process [83]. Based on the previous analysis, we consider that the implantation of external ions into the interior of the sample and the collision cascade between atoms will result in lattice distortion,

leading most atoms to be squeezed, and subsequently to residual compressive stress. Comparing Fig. 13(a)-(e), it can be observed that the increase of implantation energy is responsible for the increase in the residual compressive stress in the X-direction. When the implantation energy is 3.0 keV, the residual compressive stress reaches its maximum value of 2.1 GPa. The variation curve of the maximum residual compressive stress in the X-direction under different implantation energies is plotted in Fig. 13(f), where it can be understood that the maximum residual compressive stress in the X-direction increases analogously with the energy.

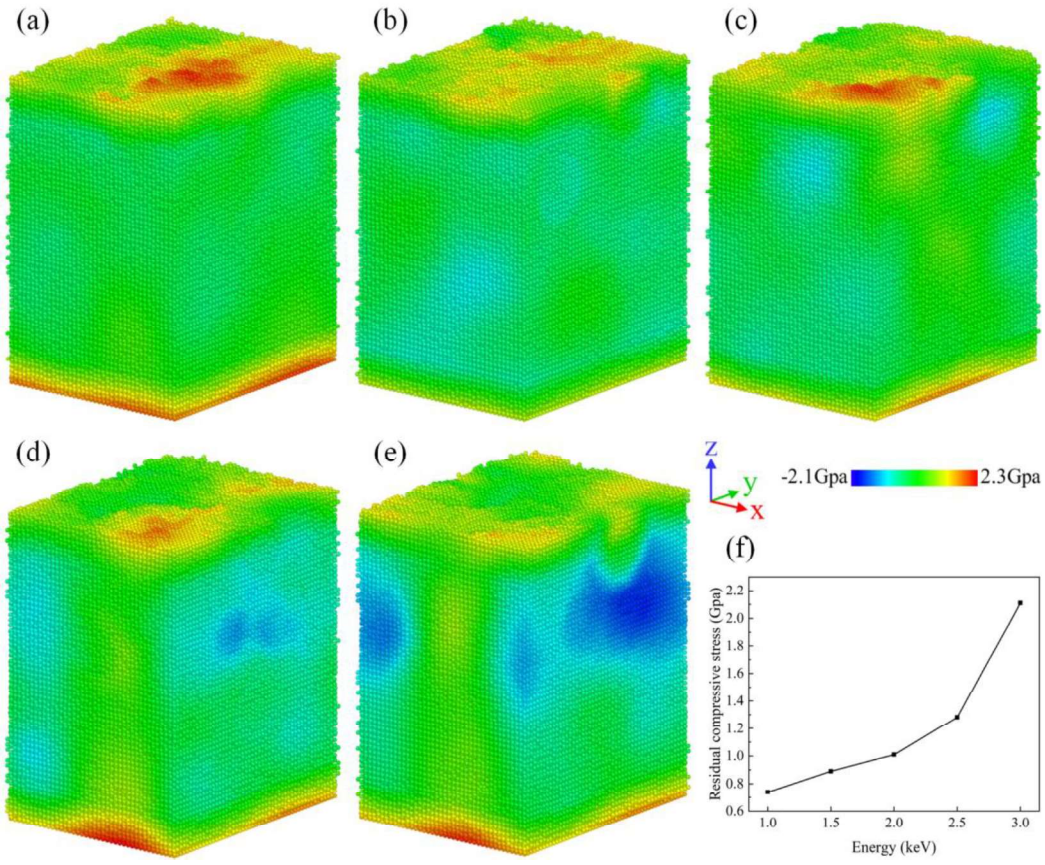

Fig. 13. Residual stress distribution cloud diagram and maximum residual compressive stress variation curve in the X direction of the sample under different energies after ion implantation. (a)-(e) Correspond to the implantation energies of 1.0 keV, 1.5 keV, 2.0 keV, 2.5 keV, and 3.0 keV respectively, and the implantation dose is 6.11×10^{13} ions/cm^2. (f) The variation curve of the maximum residual compressive stress in the X

direction under different energies.

To further reveal the underlying mechanism of residual stress generation and change, the variation curves of the X-direction average residual stress with sample depth for 1.5 keV and 3.0 keV implantation energies were plotted (see Fig. 14). It can be found that the variation curves of the average residual stress show a typical "V" shape, sharply decreasing to a global minima, followed by a smooth rise to a stable value. However, the rates of residual stress change at different energies differ, resulting in significant differences in the appearance of inflection points and residual stress stability values. From the curves and the corresponding stress cloud diagram, it can be clearly seen that the sample surface and near-surface are dominated by residual tensile stress, while residual compressive stress is concentrated mainly at the subsurface layer. This corresponds to the primary region where collision cascade and a higher amorphous rate occur after ion implantation. As the energy increases, the region of residual compressive stress expands. For an implantation energy of 1.5 keV, the depth of maximum residual compressive stress is around 50 Å, while at 3.0 keV, the maximum residual compressive stress extends to approximately 60 Å. Surprisingly, the layer of maximum residual compressive stress is slightly deeper than the corresponding average ion implantation depth, which is an indirect confirmation of an intrinsic correlation between ion implantation depth and the depth of the layer with maximum residual compressive stress.

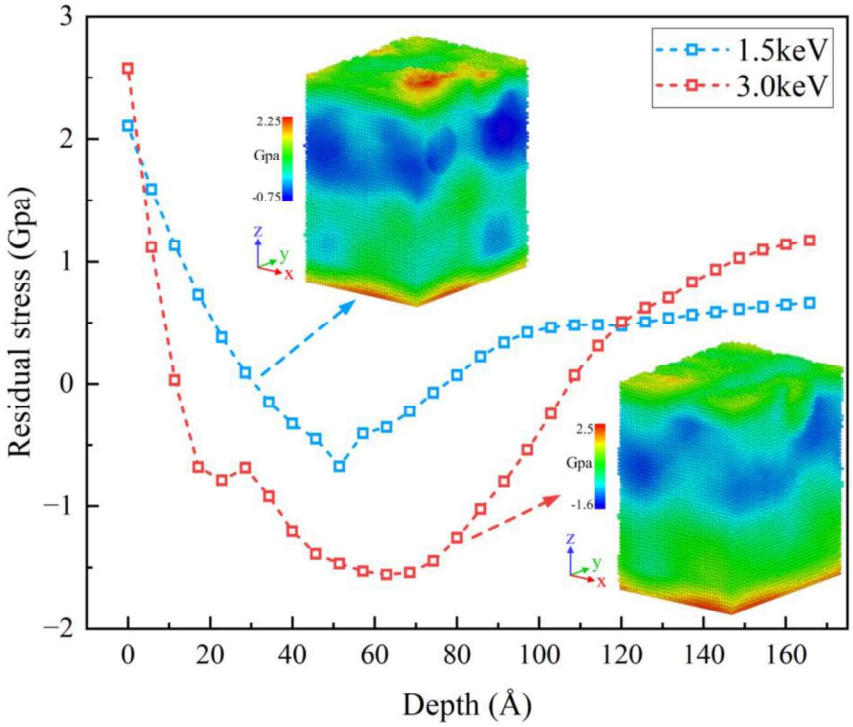

Fig. 14. The variation curve of the average residual stress in the X direction of 1.5 keV and 3.0 keV with the depth of the sample and its corresponding stress cloud diagram, the implantation dose is 6.11×10^{13} ions/cm^2.

In order to more clearly reflect the residual stresses induced by lattice distortion and phase transformation, models with implantation energies of 1.5 keV and 3.0 keV were sliced along the Y-Z plane, and the X-direction residual stress and crystal structure of the sliced planes were observed (see Fig. 15). The coordinate on the X-axis for this plane is 55 Å. By comparing the residual stress cloud diagram with the corresponding crystal structure diagram, it can be found that the region of concentrated residual compressive stress corresponds closely to the areas of amorphous structure and lattice distortion, indicating that amorphous structure and lattice distortion cause compressive stress concentration. Comparing Fig. 15(b) and (d), it can be seen that at the implantation energy of 3.0 keV more amorphous structures and more serious lattice distortion are generated (Fig. 15(d1)), and that the compressive effect is more apparent. Moreover, lattice distortions can promote the nucleation of dislocations [84]. The formation of dislocations is a significant factor in the substantial increase in maximum

compressive stress (Fig. 15(d2)), explaining why the residual compressive stress in this region is observed to be noticeably higher than other regions in Fig. 15(c).

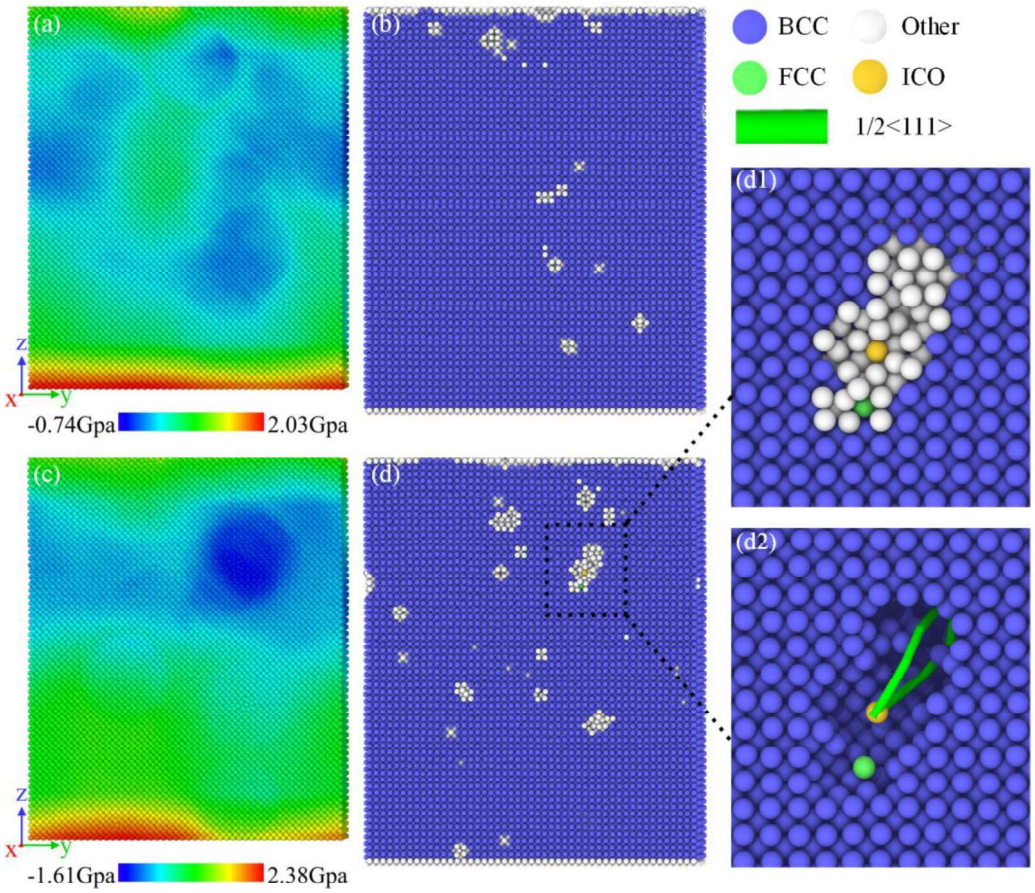

Fig. 15. X-direction residual stress cloud diagram and corresponding crystal structure diagram of the Y-Z plane when the X-axis coordinate is 55 Å. (a)-(b) Correspond to an implantation energy of 1.5 keV and an implantation dose of 6.11×10^{13} ions/cm^2. (c)-(d) Correspond to an implantation energy of 3.0 keV and an implantation dose of 6.11×10^{13} ions/cm^2, (d1)-(d2) are enlarged views of the crystal structure and dislocation at the same local position.

Annealing has the potential to alter various properties of materials [85]. To evaluate the effect of annealing after ion implantation on residual compressive stress, the peak residual compressive stress in the X direction before and after annealing is plotted in Fig. 16. Clearly, before annealing, the sample has a large peak residual

compressive stress in the X direction. After annealing, the peak residual compressive stress is markedly reduced to a lower level. This is because annealing can repair the lattice structure, but amorphous regions that are challenging to repair still exist [46]. Before annealing, the peak residual compressive stress shows obvious differences due to the increase of energy. However, after annealing, the peak residual compressive stress at different energies is relatively close, which is attributed to the fact that more amorphous atoms can facilitate heat dissipation in the high-energy region during annealing, thereby releasing more residual compressive stress in the same annealing time [21].

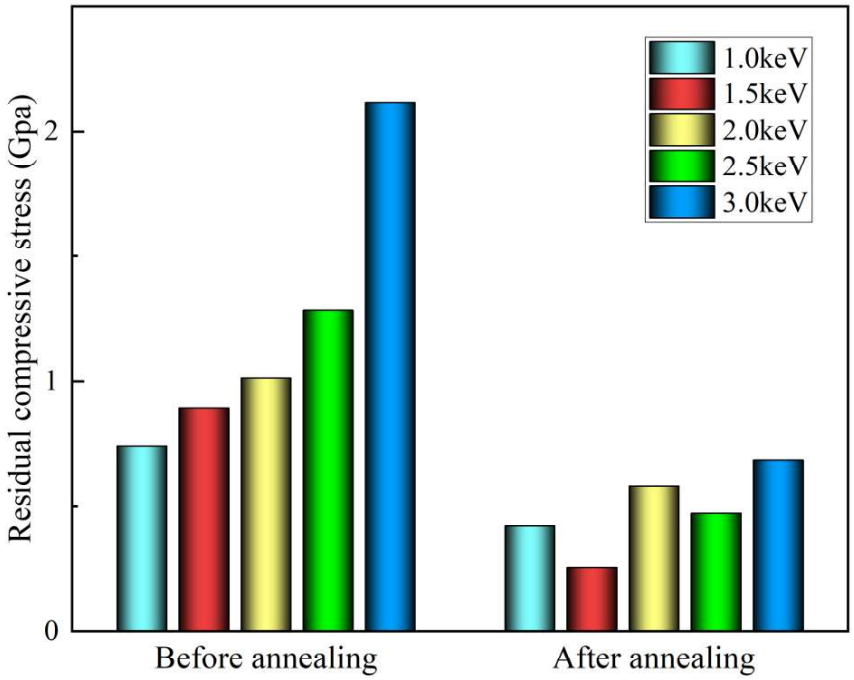

Fig. 16. Peak residual compressive stress in X direction before and after annealing at different implantation energies, and the implantation dose is 6.11×10^{13} ions/cm^2.

4. Conclusions

This study employed molecular dynamics simulations to model the ion implantation process of Cr ions into single-crystal iron, thoroughly investigating the nanoscale structural evolution and modification mechanisms across varying energies and doses. The main conclusions include.

Ion implantation of Cr alters the surface morphology of the sample, leading to the formation of bulges and pits. The surface roughness demonstrates an upward trend as the implantation energy and dose escalate. Notably, the augmentation in energy exerts a more pronounced effect on surface roughness than does an increase in dose. Moreover, energy also plays a key role in regulating the depth and breadth of the modified layer. At an energy level of 1.0 keV, a modified layer with a thickness of approximately 2 nm is created.

The saturation dose and the equilibrium values of vacancies and interstitial atoms largely depend on the energy of implantation. In the initial phase of ion implantation, the sputtering yield is notably high. However, with increasing doses, it exhibits gradual fluctuations before stabilizing. At an implantation energy of 3.0 keV, marked thermal spike effects and recrystallization phenomena are observed.

The notable expansion of the amorphous region's volume is directly correlated with the rise in implantation energy. Within this modified region, clusters of high-density amorphous material are formed. Once the dose reaches 1.53×10^{13} ions/cm^2, the quantity of amorphous atoms changes from initial linear growth to a slow increase until reaching saturation. Furthermore, an implantation energy of 2.0 keV has been identified as a critical threshold influencing the alteration in the number of amorphous atoms and the transformation of the crystal structure.

Ion implantation can induce the formation of dislocations, a process influenced not only by the implantation energy but also by the dose. The correlation between the average dislocation length and the implantation energy is notable. Throughout the ion implantation process, 1/2<111> dislocation loops progressively glide in a direction parallel to the Burgers vector, moving towards the surface where they eventually annihilate. In this movement, they can also merge with other dislocation loops to form larger ones. Additionally, <100> dislocation loops may react to produce 1/2<111> dislocation loops.

Residual compressive stress is primarily induced by lattice distortion and phase transformation, its magnitude and depth increase with the increase in energy. Moreover, annealing helps to reduce residual compressive stress.

Acknowledgements

The authors gratefully acknowledge the support of the National Key R&D Program of China (Grant No. 2023YFB3406404); the support of the Defense Industrial Technology Development Program (Grants No. JCKY2020213B006); the National Key Laboratory of Science and Technology on Helicopter Transmission (Grant No. HTL-0-21G04).

Author contributions

Jiangping Zhu: Methodology, Software, Visualization, Writing – original draft, Writing – review & editing. Wen Shao: Funding acquisition, Methodology, Writing – review & editing. Weiwei Huang: Methodology, Software, Writing – review & editing. Jinyuan Tang: Resources, Supervision, Writing – review & editing. Tingting Jiang: Conceptualization, Validation. Yuansheng Zhou: Investigation. Xiaocheng Shen: Software. Dimitrios Kontziampasis: Writing – review & editing.

Data and code availability

Data will be made available on request.

Conflicts of interest

The authors declare that they have no known competing financial interests or personal relationships that could have appeared to influence the work reported in this paper.

References

[1] S.V. Trukhanov, A.V. Trukhanov, V.A. Turchenko, V.G. Kostishin, L.V. Panina, I.S. Kazakevich, A.M. Balagurov, Crystal structure and magnetic properties of the BaFe12−xInxO19 (x=0.1 ‐ 1.2) solid solutions, J. Magn. Magn. Mater., 417 (2016) 130-136.https://doi.org/https://doi.org/10.1016/j.jmmm.2016.05.052.

[2] A.V. Trukhanov, K.A. Darwish, M.M. Salem, O.M. Hemeda, M.I. Abdel Ati, M.A. Darwish, E.Y. Kaniukov, S.V. Podgornaya, V.A. Turchenko, D.I. Tishkevich, T.I. Zubar, K.A. Astapovich, V.G. Kostishyn, S.V. Trukhanov, Impact of the heat treatment conditions on crystal structure, morphology and magnetic properties evolution in BaM nanohexaferrites, J. Alloys Compd., 866 (2021) 158961.https://doi.org/https://doi.org/10.1016/j.jallcom.2021.158961.

[3] R.E. El-Shater, H. El Shimy, S.A. Saafan, M.A. Darwish, D. Zhou, A.V. Trukhanov, S.V. Trukhanov, F. Fakhry, Synthesis, characterization, and magnetic properties of Mn nanoferrites, J. Alloys Compd., 928 (2022) 166954.https://doi.org/https://doi.org/10.1016/j.jallcom.2022.166954.

[4] T. Zubar, V. Fedosyuk, D. Tishkevich, O. Kanafyev, K. Astapovich, A. Kozlovskiy, M. Zdorovets, D. Vinnik, S. Gudkova, E. Kaniukov, A.S.B. Sombra, D. Zhou, R.B.

Jotania, C. Singh, S. Trukhanov, A. Trukhanov, The Effect of Heat Treatment on the Microstructure and Mechanical Properties of 2D Nanostructured Au/NiFe System, Nanomaterials, 10 (2020) 1077.https://doi.org/https://doi.org/10.3390/nano10061077.
[5] D.O. Shpylka, I.V. Ovsiienko, T.A. Len, L.Y. Matzui, S.V. Trukhanov, A.V. Trukhanov, O.S. Yakovenko, The features of the magnetoresistance of carbon nanotubes modified with Fe, Ceram. Int., 48 (2022) 19789-19797.https://doi.org/https://doi.org/10.1016/j.ceramint.2022.03.253.
[6] O.S. Yakovenko, L.Y. Matzui, L.L. Vovchenko, V.V. Oliynyk, V.V. Zagorodnii, S.V. Trukhanov, A.V. Trukhanov, Electromagnetic Properties of Carbon Nanotube/BaFe12−xGaxO19/Epoxy Composites with Random and Oriented Filler Distributions, Nanomaterials, 11 (2021) 2873.https://doi.org/https://doi.org/10.3390/nano11112873.
[7] W. Ye, Q. Zhou, Y. Shi, M. Xie, B. Chen, H. Wang, W. Liu, Robust wear performance of graphene-reinforced high entropy alloy composites, Carbon, 224 (2024) 119040.https://doi.org/https://doi.org/10.1016/j.carbon.2024.119040.
[8] I.P. Jain, G. Agarwal, Ion beam induced surface and interface engineering, Surf. Sci. Rep., 66 (2011) 77-172.https://doi.org/https://doi.org/10.1016/j.surfrep.2010.11.001.
[9] J. Jin, Y. Chen, K. Gao, X. Huang, The effect of ion implantation on tribology and hot rolling contact fatigue of Cr4Mo4Ni4V bearing steel, Appl. Surf. Sci., 305 (2014) 93-100.https://doi.org/https://doi.org/10.1016/j.apsusc.2014.02.174.
[10] J. Jin, T. Shao, Effects of single- and dual-element ion implantation on tribomechanical properties of Cronidur 30 bearing steel, Surf. Coat. Technol., 344 (2018) 303-311.https://doi.org/10.1016/j.surfcoat.2018.03.033.
[11] N. Levintant-Zayonts, G. Starzynski, S. Kucharski, Effect of N ion implantation on tribological properties of spring steels, Appl. Surf. Sci., 591 (2022).https://doi.org/10.1016/j.apsusc.2022.153117.
[12] D. Wei, F. Li, S. Li, S. Wang, F. Ding, T. Tian, P. Zhang, Z. Yao, Effect of Cr ion implantation on surface morphology, lattice deformation, nanomechanical and fatigue behavior of TC18 alloy, Appl. Surf. Sci., 506 (2020) 145023.https://doi.org/https://doi.org/10.1016/j.apsusc.2019.145023.
[13] A.I. Ryabchikov, E.B. Kashkarov, A.E. Shevelev, A. Obrosov, D.O. Sivin, Surface modification of Al by high-intensity low-energy Ti-ion implantation: Microstructure, mechanical and tribological properties, Surf. Coat. Technol., 372 (2019) 1-8.https://doi.org/10.1016/j.surfcoat.2019.05.020.
[14] H. Wang, Y. Zheng, C. Jiang, Y. Li, Y. Fu, In vitro corrosion behavior and cytocompatibility of pure Fe implanted with Ta, Surf. Coat. Technol., 320 (2017) 201-205.https://doi.org/10.1016/j.surfcoat.2017.01.051.
[15] T. Chen, E. Castanon, J.G. Gigax, H. Kim, R. Balerio, J. Fan, F.A. Garner, L. Shao, Nitrogen ion implantation into pure iron for formation of surface nitride layer, Nucl. Instrum. Methods Phys. Res. Sect. B-Beam Interact. Mater. Atoms, 451 (2019) 10-13.https://doi.org/10.1016/j.nimb.2019.04.033.
[16] T. Rüdiger, M. Mitzschke, A. Prager, Y. Liu, B. Abel, A. Schulze, F. Frost, Ion incidence angle dependent pattern formation at AZ 4562® photo resist by Ar+ ion beam erosion, Appl. Surf. Sci., 574 (2022)

151682.https://doi.org/https://doi.org/10.1016/j.apsusc.2021.151682.
[17] G. Yang, D. Hirsch, J. Li, Y. Liu, F. Frost, Y. Hong, Energy dependence of morphologies on photoresist surfaces under Ar+ ion bombardment with normal incidence, Appl. Surf. Sci., 523 (2020) 146510.https://doi.org/https://doi.org/10.1016/j.apsusc.2020.146510.
[18] E. Gogolides, V. Constantoudis, G. Kokkoris, D. Kontziampasis, K. Tsougeni, G. Boulousis, M. Vlachopoulou, A. Tserepi, Controlling roughness: from etching to nanotexturing and plasma-directed organization on organic and inorganic materials, J. Phys. D: Appl. Phys., 44 (2011) 174021.https://doi.org/10.1088/0022-3727/44/17/174021.
[19] N. Vourdas, D. Kontziampasis, G. Kokkoris, V. Constantoudis, A. Goodyear, A. Tserepi, M. Cooke, E. Gogolides, Plasma directed assembly and organization: bottom-up nanopatterning using top-down technology, Nanotechnology, 21 (2010) 085302.https://doi.org/10.1088/0957-4484/21/8/085302.
[20] A. Arapis, V. Constantoudis, D. Kontziampasis, A. Milionis, C.W.E. Lam, A. Tripathy, D. Poulikakos, E. Gogolides, Measuring the complexity of micro and nanostructured surfaces, Materials Today: Proceedings, 54 (2022) 63-72.https://doi.org/https://doi.org/10.1016/j.matpr.2021.10.120.
[21] Q. Kang, X. Fang, C. Wu, H. Sun, B. Tian, L. Zhao, S. Wang, Z. Jiang, N. Zhu, R. Maeda, M. Zhang, Y. Lv, Modification mechanism of collaborative ions implanted into 4H-SiC by atomic simulation and experiment, Int. J. Mech. Sci., 212 (2021).https://doi.org/10.1016/j.ijmecsci.2021.106832.
[22] W. Huang, J. Tang, W. Zhou, W. Shao, M. Yi, X. Zhao, J. Wen, Revealing nanoscale material deformation mechanism and surface/subsurface characteristics in vibration-assisted nano-grinding of single-crystal iron, Appl. Surf. Sci., 597 (2022).https://doi.org/10.1016/j.apsusc.2022.153692.
[23] W. Wu, Y. Hu, X. Meng, J. Dai, H. Dai, Molecular dynamics simulation of ion-implanted single-crystal 3C-SiC nano-indentation, J. Manuf. Process., 79 (2022) 356-368.https://doi.org/10.1016/j.jmapro.2022.04.071.
[24] Y.J. Xiao, F.Z. Fang, Z.W. Xu, X.T. Hu, Annealing recovery of nanoscale silicon surface damage caused by Ga focused ion beam, Appl. Surf. Sci., 343 (2015) 56-69.https://doi.org/10.1016/j.apsusc.2015.03.059.
[25] Z. Xu, L. Liu, Z. He, D. Tian, A. Hartmaier, J. Zhang, X. Luo, M. Rommel, K. Nordlund, G. Zhang, F. Fang, Nanocutting mechanism of 6H-SiC investigated by scanning electron microscope online observation and stress-assisted and ion implant-assisted approaches, Int. J. Adv. Manuf. Technol., 106 (2020) 3869-3880.https://doi.org/10.1007/s00170-019-04886-6.
[26] B. Liu, Z. Xu, Y. Wang, X. Gao, R. Kong, Effect of ion implantation on material removal mechanism of 6H-SiC in nano-cutting: A molecular dynamics study, Comput. Mater. Sci., 174 (2020).https://doi.org/10.1016/j.commatsci.2019.109476.
[27] H. Dai, Y. Hu, W. Wu, H. Yue, X. Meng, P. Li, H. Duan, Molecular dynamics simulation of ultra-precision machining 3C-SiC assisted by ion implantation, J. Manuf. Process., 69 (2021) 398-411.https://doi.org/10.1016/j.jmapro.2021.07.055.
[28] Y. Fan, Z. Xu, Y. Song, B. Dong, Z. Xue, B. Liu, L. Liu, D. Tian, Nano material

removal mechanism of 4H-SiC in ion implantation-assisted machining, Comput. Mater. Sci., 200 (2021).https://doi.org/10.1016/j.commatsci.2021.110837.
[29] Q. Kang, X. Fang, C. Wu, H. Sun, Z. Fang, B. Tian, L. Zhao, S. Wang, N. Zhu, P. Verma, M. Ryutaro, Z. Jiang, Improvement mechanism of brittle-plastic transition and residual stress in scratching 4H-SiC implanted by hydrogen ions, Ceram. Int., 48 (2022) 27076-27087.https://doi.org/10.1016/j.ceramint.2022.06.019.
[30] W. Wu, Y. Hu, X. Meng, B. Liao, H. Dai, Molecular dynamics analysis of the influence of ion implantation parameters on ultra-precision machining of silicon carbide, J. Manuf. Process., 82 (2022) 174-191.https://doi.org/10.1016/j.jmapro.2022.07.059.
[31] M. Lebeda, J. Drahokoupil, P. Vertat, P. Vlcak, Quantifying low-energy nitrogen ion channeling in α-titanium by molecular dynamics simulations, Mater. Chem. Phys., 306 (2023).https://doi.org/10.1016/j.matchemphys.2023.128098.
[32] M. Zhang, J. Chen, K. Sun, L. Fang, The effect of point defects caused by particle bombardment on the deformation behaviours of alpha-iron: A molecular dynamics simulation, Mater. Chem. Phys., 241 (2020).https://doi.org/10.1016/j.matchemphys.2019.122414.
[33] T. Jiang, J. Tang, J. Zhao, J. Zhu, X. Shen, MD simulation study on the microstructural evolution of single-crystal Fe with pre-existing defects by Cr ion implantation, Surf. Interfaces, 44 (2024) 103651.https://doi.org/https://doi.org/10.1016/j.surfin.2023.103651.
[34] J. Taghinejad, A.R. Niknam, M.R. Ghahyazi, A. Moradkhani, Molecular dynamics simulations of Ar plus bombardment of Fe(0,0,1), (1,0,1), and (1,1,1) surfaces: Study of threshold energy and angular characteristics of sputtering, Vacuum, 215 (2023).https://doi.org/10.1016/j.vacuum.2023.112312.
[35] D.-H. Kim, D.H. Kim, Sputtering of Fe(100) due to low-energy ion bombardments: Molecular dynamics simulation, Scripta Mater., 55 (2006) 1043-1046.https://doi.org/10.1016/j.scriptamat.2006.08.006.
[36] Q. Peng, F. Meng, Y. Yang, C. Lu, H. Deng, L. Wang, S. De, F. Gao, Shockwave generates <100> dislocation loops in bcc iron, Nat. Commun., 9 (2018).https://doi.org/10.1038/s41467-018-07102-3.
[37] F. Granberg, J. Byggmastar, K. Nordlund, Molecular dynamics simulations of high-dose damage production and defect evolution in tungsten, J. Nucl. Mater., 556 (2021).https://doi.org/10.1016/j.jnucmat.2021.153158.
[38] J. Wu, F. Granberg, Simulation of defect build-up in tungsten during low energy irradiation, J. Nucl. Mater., 586 (2023).https://doi.org/10.1016/j.jnucmat.2023.154653.
[39] S. Plimpton, Fast Parallel Algorithms for Short-Range Molecular Dynamics, J. Comput. Phys., 117 (1995) 1-19.https://doi.org/https://doi.org/10.1006/jcph.1995.1039.
[40] A. Stukowski, Visualization and analysis of atomistic simulation data with OVITO-the Open Visualization Tool, Modell. Simul. Mater. Sci. Eng., 18 (2010).https://doi.org/10.1088/0965-0393/18/1/015012.
[41] H. Hijazi, M. Li, D. Barbacci, A. Schultz, R. Thorpe, T. Gustafsson, L.C. Feldman, Channeling in the helium ion microscope, Nucl. Instrum. Methods Phys. Res. Sect. B-Beam Interact. Mater. Atoms, 456 (2019) 92-

96.https://doi.org/10.1016/j.nimb.2019.07.002.
[42] W. Zhao, Z. Xu, F. Ren, B. Dong, J. Zhao, P. Wang, Enhancing the fabrication yield of NV centers in diamond by pre-doping using molecular dynamics simulation, Diamond Relat. Mater., 132 (2023).https://doi.org/10.1016/j.diamond.2023.109683.
[43] X.-X. Guo, J.-L. Shao, G. Lu, Reversibility of the structural transition in single crystal iron driven by uniaxial and triaxial strains: Atomistic study, Int. J. Mech. Sci., 191 (2021).https://doi.org/10.1016/j.ijmecsci.2020.106064.
[44] J.E. Basconi, M.R. Shirts, Effects of Temperature Control Algorithms on Transport Properties and Kinetics in Molecular Dynamics Simulations, J. Chem. Theory Comput., 9 (2013) 2887-2899.https://doi.org/10.1021/ct400109a.
[45] J. Guenole, A. Prakash, E. Bitzek, Atomistic simulations of focused ion beam machining of strained silicon, Appl. Surf. Sci., 416 (2017) 86-95.https://doi.org/10.1016/j.apsusc.2017.04.027.
[46] Y. Fan, Z. Xu, Y. Song, T. Sun, Molecular dynamics simulation of silicon vacancy defects in silicon carbide by hydrogen ion implantation and subsequent annealing, Diamond Relat. Mater., 119 (2021).https://doi.org/10.1016/j.diamond.2021.108595.
[47] G. Wei, F. Ren, W. Qin, W. Hu, H. Deng, C. Jiang, Evolution of helium bubbles below different tungsten surfaces under neutron irradiation and non-irradiation conditions, Comput. Mater. Sci., 148 (2018) 242-248.https://doi.org/10.1016/j.commatsci.2018.02.050.
[48] D. Frenkel, B. Smit, Understanding molecular simulation: from algorithms to applications, Elsevier, 2023.
[49] M.I. Mendelev, S. Han, D.J. Srolovitz, G.J. Ackland, D.Y. Sun, M. Asta, Development of new interatomic potentials appropriate for crystalline and liquid iron, Philos. Mag., 83 (2003) 3977-3994.https://doi.org/10.1080/14786430310001613264.
[50] B. Beeler, M. Asta, P. Hosemann, N. Gronbech-Jensen, Effects of applied strain on radiation damage generation in body centered cubic iron, J. Nucl. Mater., 459 (2015) 159-165.https://doi.org/10.1016/j.jnucmat.2014.12.111.
[51] Q.-u.-a. Sahi, Y.-S. Kim, Primary radiation damage characterization of α-iron under irradiation temperature for various PKA energies, Mater. Res. Express, 5 (2018).https://doi.org/10.1088/2053-1591/aabb6f.
[52] P. Kuopanportti, M. Ropo, D. Holmberg, H. Levamaki, K. Kokko, S. Granroth, A. Kuronen, Interatomic Fe-Cr potential for modeling kinetics on Fe surfaces, Comput. Mater. Sci., 203 (2022).https://doi.org/10.1016/j.commatsci.2021.110840.
[53] Tersoff, Modeling solid-state chemistry: Interatomic potentials for multicomponent systems, Phys. Rev. B-Condens Matter, 39 (1989) 5566-5568.https://doi.org/10.1103/PhysRevB.39.5566.
[54] J.F. Ziegler, J.P. Biersack, The Stopping and Range of Ions in Matter, in: D.A. Bromley (Ed.) Treatise on Heavy-Ion Science: Volume 6: Astrophysics, Chemistry, and Condensed Matter, Springer US, Boston, MA, 1985, pp. 93-129.
[55] Y. Chen, X. Liao, R. Qiu, L. Liu, W. Hu, H. Deng, Primary radiation damage in tungsten-based high-entropy alloy: Interatomic potential and collision cascade simulations, J. Nucl. Mater., 585 (2023).https://doi.org/10.1016/j.jnucmat.2023.154646.
[56] J.F. Ziegler, M.D. Ziegler, J.P. Biersack, SRIM - The stopping and range of ions in

matter (2010), Nucl. Instrum. Methods Phys. Res. Sect. B-Beam Interact. Mater. Atoms, 268 (2010) 1818-1823.https://doi.org/10.1016/j.nimb.2010.02.091.
[57] J. Wu, Z. Xu, L. Liu, A. Hartmaier, M. Rommel, K. Nordlund, T. Wang, R. Janisch, J. Zhao, MD simulation study on defect evolution and doping efficiency of p-type doping of 3C-SiC by Al ion implantation with subsequent annealing, J. Mater. Chem. C, 9 (2021).https://doi.org/10.1039/d0tc05374k.
[58] F. Liu, G. Fu, Y. Cui, Q. Sun, M. Qu, Y. Sun, Tribological properties and surface structures of ion implanted 9Cr18Mo stainless steels, Nucl. Instrum. Methods Phys. Res. Sect. B-Beam Interact. Mater. Atoms, 307 (2013) 412-418.https://doi.org/10.1016/j.nimb.2012.12.115.
[59] M.A. Alam, M.K. Tiwari, D. Devi, S. Tripathi, A. Trivedi, S. Ojha, R. Singh, M. Gupta, Depth profile analysis of 100 keV Ni ions in Si <100> substrate, Spectroc. Acta Pt. B-Atom. Spectr., 206 (2023).https://doi.org/10.1016/j.sab.2023.106707.
[60] S. Liang, L. Zhang, H. Deng, Theoretical and experimental study on plasma-induced atom-migration manufacturing (PAMM) of glass, Appl. Surf. Sci., 599 (2022).https://doi.org/10.1016/j.apsusc.2022.153976.
[61] V.A. Turchenko, S.V. Trukhanov, V.G. Kostishin, F. Damay, F. Porcher, D.S. Klygach, M.G. Vakhitov, D. Lyakhov, D. Michels, B. Bozzo, I. Fina, M.A. Almessiere, Y. Slimani, A. Baykal, D. Zhou, A.V. Trukhanov, Features of structure, magnetic state and electrodynamic performance of SrFe12−xInxO19, Sci Rep, 11 (2021) 18342.https://doi.org/10.1038/s41598-021-97684-8.
[62] K. Lu, L. Lu, S. Suresh, Strengthening Materials by Engineering Coherent Internal Boundaries at the Nanoscale, Science, 324 (2009) 349-352.https://doi.org/10.1126/science.1159610.
[63] Y. Ren, Q. Zhou, D. Hua, Z. Huang, Y. Li, Q. Jia, P. Gumbsch, C. Greiner, H. Wang, W. Liu, Wear-resistant CoCrNi multi-principal element alloy at cryogenic temperature, Science Bulletin, 69 (2024) 227-236.https://doi.org/https://doi.org/10.1016/j.scib.2023.12.003.
[64] S.V. Trukhanov, Peculiarities of magnetic phase separation in anion-deficient La0.70Sr0.30MnO2.85 manganite, Physics of the Solid State, 53 (2011) 1845-1850.https://doi.org/10.1134/S1063783411090307.
[65] K.Y. Fung, Y.R. Lin, P.J. Yu, J.J. Kai, A. Hu, Microscopic origin of black spot defect swelling in single crystal 3C-SiC, J. Nucl. Mater., 508 (2018) 292-298.https://doi.org/10.1016/j.jnucmat.2018.05.054.
[66] Z. Tong, X. Luo, Investigation of focused ion beam induced damage in single crystal diamond tools, Appl. Surf. Sci., 347 (2015) 727-735.https://doi.org/10.1016/j.apsusc.2015.04.120.
[67] Y. Zhao, Y. Li, F. Yang, Z. Xie, X. Wu, Y. Wang, Irradiation performance of concentrated solid-solution alloys: Insight into defect behaviors, J. Nucl. Mater., 583 (2023).https://doi.org/10.1016/j.jnucmat.2023.154510.
[68] M.D. Mihai, D. Iancu, E. Zarkadoula, R.A. Florin, Y. Tong, Y. Zhang, W.J. Weber, G. Velisa, Athermal annealing of pre-existing defects in crystalline silicon, Acta Mater., 261 (2023).https://doi.org/10.1016/j.actamat.2023.119379.
[69] T. Sun, Z. Xu, J. Wu, Y. Fan, F. Ren, Y. Song, L. Yang, P. Tan, Divacancy and

silicon vacancy color centers in 4H-SiC fabricated by hydrogen and dual ions implantation and annealing, Ceram. Int., 49 (2023) 7452-7465.https://doi.org/10.1016/j.ceramint.2022.10.219.
[70] J. Kirschner, H.W. Etzkorn, On the fluence dependence of the sputtering yield for low-energy noble gas ions, Appl. Phys. A, 29 (1982) 133-139.https://doi.org/10.1007/BF00617769.
[71] Burnett, Pellin, Calaway, Gruen, Yates, Jr., Ion dose dependence of the sputtering yield of Ru(0001) at very low fluences, Phys. Rev. Lett., 63 (1989) 562-565.https://doi.org/10.1103/PhysRevLett.63.562.
[72] R. Xu, M. Zhou, X. Wang, S.Y. Matharage, J.D. Yan, A. Connolly, Y. Luo, Y. Ding, Z. Wang, A molecular dynamics simulation study on the role of graphene in enhancing the arc erosion resistance of Cu metal matrix, Comput. Mater. Sci., 212 (2022).https://doi.org/10.1016/j.commatsci.2022.111549.
[73] H. Gnaser, Processes in low-energy ion-surface collisions: preferential sputtering, defect and adatom formation, Appl. Surf. Sci., 100-101 (1996) 316-328.https://doi.org/https://doi.org/10.1016/0169-4332(96)00234-6.
[74] J. Burnett, J. Biersack, D. Gruen, B. Jo/rgensen, A. Krauss, M. Pellin, E. Schweitzer, J. Yates Jr, C. Young, Depth of origin of sputtered atoms: experimental and theoretical study of Cu/Ru (0001), J. Vac. Sci. Technol. A-Vac. Surf. Films, 6 (1988) 2064-2068.https://doi.org/https://doi.org/10.1116/1.575604.
[75] G. Betz, M.J. Pellin, J.W. Burnett, D.M. Gruen, Low primary ion fluence dependence of single crystal sputtering: a molecular dynamics study, Nucl. Instrum. Methods Phys. Res. Sect. B-Beam Interact. Mater. Atoms, 58 (1991) 429-437.https://doi.org/https://doi.org/10.1016/0168-583X(91)95881-D.
[76] B. Deng, Y. Tao, H. Liu, P. Liu, Influence of niobium ion implantation on the microstructure and tribological properties of TiAlN coatings, Surf. Coat. Technol., 228 (2013) S554-S557.https://doi.org/10.1016/j.surfcoat.2012.04.022.
[77] J. Chen, F. Zhang, S. Yan, G. Yu, J. He, F. Yin, Effect of Ti content and annealing on microstructure and mechanical performance of plasma sprayed Ti-Al-C based composite coatings, Vacuum, 209 (2023).https://doi.org/10.1016/j.vacuum.2023.111817.
[78] Y.P. Sharkeev, E.V. Kozlov, A.N. Didenko, S.N. Kolupaeva, N.A. Vihor, The mechanisms of the long-range effect in metals and alloys by ion implantation, Surf. Coat. Technol., 83 (1996) 15-21.https://doi.org/https://doi.org/10.1016/0257-8972(95)02777-7.
[79] Y.P. Sharkeev, E.V. Kozlov, The long-range effect in ion implanted metallic materials: dislocation structures, properties, stresses, mechanisms, Surf. Coat. Technol., 158 (2002) 219-224.https://doi.org/10.1016/s0257-8972(02)00212-8.
[80] A. Stukowski, V.V. Bulatov, A. Arsenlis, Automated identification and indexing of dislocations in crystal interfaces, Modell. Simul. Mater. Sci. Eng., 20 (2012).https://doi.org/10.1088/0965-0393/20/8/085007.
[81] R. Qiu, Y. Chen, N. Gao, X. He, Y. Dou, W. Yang, W. Hu, H. Deng, Molecular dynamics simulations of displacement cascades in vanadium: Generation and types of dislocation loops, Nucl. Mater. Energy, 34

(2023).https://doi.org/10.1016/j.nme.2023.101394.
[82] K. Arakawa, K. Ono, M. Isshiki, K. Mimura, M. Uchikoshi, H. Mori, Observation of the one-dimensional diffusion of nanometer-sized dislocation loops, Science, 318 (2007) 956-959.https://doi.org/10.1126/science.1145386.
[83] K. Jacobus, R.E. DeVor, S.G. Kapoor, Machining-induced residual stress: Experimentation and modeling, J. Manuf. Sci. Eng.-Trans. ASME, 122 (2000) 20-31.https://doi.org/10.1115/1.538906.
[84] D. Hua, Q. Zhou, Y. Shi, S. Li, K. Hua, H. Wang, S. Li, W. Liu, Revealing the deformation mechanisms of 〈110〉 symmetric tilt grain boundaries in CoCrNi medium-entropy alloy, Int. J. Plast., 171 (2023) 103832.https://doi.org/https://doi.org/10.1016/j.ijplas.2023.103832.
[85] S.V. Trukhanov, A.V. Trukhanov, C.E. Botez, A.H. Adair, H. Szymczak, R. Szymczak, Phase separation and size effects in Pr0.70Ba0.30MnO3+δ perovskite manganites, J. Phys.: Condens. Matter, 19 (2007) 266214.https://doi.org/10.1088/0953-8984/19/26/266214.